LABEL-FREE MULTIPHOTON MICROSCOPY WITH A VISIBLE, FEMTOSECOND PULSED LASER SOURCE

by

Ryan Knox

Copyright © Ryan Knox 2022

A Thesis Submitted to the Faculty of the

COLLEGE OF OPTICAL SCIENCES

In Partial Fulfillment of the Requirements

For the Degree of

MASTER OF SCIENCE

In the Graduate College

THE UNIVERSITY OF ARIZONA

2022

THE UNIVERSITY OF ARIZONA
GRADUATE COLLEGE

As members of the Master's Committee, we certify that we have read the thesis prepared by **Ryan Jacob Knox**, titled ***Label-Free Multiphoton Microscopy with a Visible, Femtosecond Pulsed Laser Source*** and recommend that it be accepted as fulfilling the dissertation requirement for the Master's Degree.

Professor Khanh Q. Kieu Date: 05/04/2022

Professor R. Jason Jones Date: 5/4/2022

Professor Arthur C. Riegel Date: 4 2022

Final approval and acceptance of this thesis is contingent upon the candidate's submission of the final copies of the thesis to the Graduate College.

I hereby certify that I have read this thesis prepared under my direction and recommend that it be accepted as fulfilling the Master's requirement.

Professor Khanh Q. Kieu Date: 05/04/2022
Master's Thesis Committee Chair
Wyant College of Optical Sciences

Acknowledgements

There are many people that I would like to thank for helping me finish this work and get to this point in my life. I would first like to thank my advisor, Dr. Khanh Kieu, for always being excited about the work that I was doing. It was very inspiring and pushed me to try and do my absolute best. You have taught me so many lessons on how to be a better engineer that I will apply throughout my career. I am grateful for Dr. Jones and Dr. Riegel for taking the time to review my work and give me feedback. I hope this work will allow for more collaboration in the future.

Next, I would like to thank all of my past and current lab mates from my time working in the Ultrafast Fiber Laser and Nonlinear Optics Group. A special thanks to Dr. Benjamin Cromey, who I first met as a sophomore in the College of Optical Sciences. You have taught me so much about optics, the engineering industry, and more. You took a genuine interest in watching me grow as an engineer and taught me countless lessons along the way. I will always be grateful for the opportunity to work with you in lab and in senior design. Dr. Orkhongua Batjargal for starting this project and answering any questions that I had along the way. I would have been lost in the beginning if it weren't for your help explaining the work that you had done on this project. You also helped the laser and microscope come together by answering any questions that I had about any topic. Josh Magnus for always being in the lab and giving me feedback on results that I obtained. You helped at critical points in the laser building process by teaching me good techniques and assisting with tough measurements. Our conversations when I was building and analyzing the detection system to the microscope directly lead to the results shown in this paper. Lam Nguyen for offering me a helping hand whenever you could. I hope you enjoy the PhD program and if you choose to continue working on this project, I know it is in good hands.

I would like to thank all of my friends that I made during my undergraduate and graduate years at the University of Arizona. You are all a part of memories that I will cherish for a lifetime.

Next, I would like to thank my family. My grandparents, Fred, Linda, Dennis, and Janet for the unconditional support. My siblings, Adam and Allie for tolerating me through the years. It's crazy to think that we'll all be in different states doing our own thing soon. My parents, Ken and Julie for providing me with endless opportunities to get me to this point in my life. You have both supported me through all of my adventures and constantly inspire me to be the best that I can be.

Lastly, I would like to thank my girlfriend Noelle for always encouraging me and having my back. At times during this process when I had late nights and didn't think I'd be able to finish my work you were always there to lift my sprits and tell me that I could do anything. I'm very excited to see where life takes us!

Table of Contents

List of Figures

Abstract

Multiphoton microscopy is commonly used as a tool in biological and material science. Using a high peak power, ultrafast source, a multiphoton microscope (MPM) can detect nonlinear optical signals that allow for label-free contrast and depth-resolved imaging. Commercial multiphoton systems use tunable Ti:Sapphire lasers in the near-infrared (NIR), which can be very large, expensive, and difficult to operate. The Ultrafast Fiber Lasers and Nonlinear Optics group at the Wyant College of Optical Sciences has developed many compact, robust, easy to use NIR fiber laser sources with comparable performance to the Ti:Sapphire laser for applications in multiphoton microscopy. In this thesis, a multiphoton microscope is designed using a visible laser source. With higher energy photons from the source, a visible MPM has the advantages of exciting most fluorophores and imaging at a higher resolution than a typical MPM with a NIR source. The design and characterization of the source and microscope will be detailed, as well as areas for improvement and future work.

1. Introduction

1.1 Motivation

The capability of obtaining label-free signal and depth resolved images in a sample is very important and can lead to a variety of useful applications in biological and material science. A conventional brightfield microscope can produce high quality images, but the sample must be very thin and requires a contrast agent. Multiphoton microscopy, a form of laser scanning microscopy, uses nonlinear optics to both capture images at different focal planes through a relatively thick sample and to generate contrast in a sample without the need to stain [1].

Multiphoton absorption was first theoretically described in 1936 by Maria Göppert-Mayer, though it could not be physically realized until after the invention of the laser in 1960 [2,3]. Two photon excited fluorescence was first observed in a europium-doped crystal by Kaiser and Garret in 1961, and eventually the first multiphoton microscope was built in 1990 by Denk, Strickler, and Webb [3,4,5]. Multiphoton microscopy requires a tightly focused, ultrafast pulse to generate nonlinear optical signal in a sample. This pulse commonly comes from a mode locked laser and has a pulse width on the order of femtoseconds to picoseconds. When the ultrafast pulse is focused on to a sample, signal is only generated within the focal volume of the objective where the photon density is the highest [6]. Generating signal in only the focal volume of a sample is called optical sectioning, and it provides many of the advantages to multiphoton microscopy. For example, adjusting the position of the focal volume on the sample allows for nondestructive, depth resolved imaging while simultaneously reducing the effect of photobleaching [6]. In addition to three-dimensional imaging, the nonlinear optical signal has inherent contrast mechanisms which eliminates the need to stain a sample and allows for label-free contrast. The nonlinear signal detected by a multiphoton microscope will be discussed further in Section 1.3.

Commercial multiphoton systems operate using tunable Ti:Sapphire lasers, which are very large, expensive, and difficult to maintain and operate. The Ultrafast Fiber Laser and Nonlinear Optics Group at the Wyant College of Optical Sciences has designed and built many multiphoton microscope systems in house for a fraction of the size and cost of a commercial system [7,8]. These multiphoton systems operate with a femtosecond pulsed fiber laser source. The all-fiber laser format is advantageous because spliced fibers eliminate the need for

alignment, and all the optical fiber and components can be packaged in a hand-held box [9]. The microscopes built in-house have been used for many applications ranging from a tool that can help with the diagnosis of pancreatic cancer, to the characterization of gems and minerals [10,11,12].

For centuries, the goal of microscope design has been to maximize resolution to see things that are unresolvable to the human eye. The optical resolution of a microscope is dependent on the numerical aperture (NA) of the objective and the wavelength of the source, which will be discussed further in Section 1.5. Typical multiphoton laser sources operate in the NIR and can be tuned with the use of an optical parametric oscillator (OPO). While these longer source wavelengths maximize penetration depth, it is at the cost of resolution and ability to excite many fluorophores. Using existing fiber laser and multiphoton microscope technology, a visible, femtosecond pulsed laser source allows for a multiphoton microscope with the capability of imaging at a higher resolution and opens the door to many new applications in the fields of biology and material science.

1.2 Objective

The goal of this thesis is to develop a visible, femtosecond (fs) pulsed fiber laser source and multiphoton microscope that can detect ultraviolet (UV) signal. The fs pulsed source will allow non-destructive three-dimensional imaging and label-free contrast, with the shorter wavelength giving the additional advantage of higher resolution and the ability to excite most fluorophores. The source will use a combination of existing fiber technology and free space components to minimize the size, alignment, and cost compared to a commercial Ti:Sapphire laser. The microscope will also be designed using existing technology as well as standard focusing optics in the illumination path. This thesis will detail the design, characterization, and performance of the laser and microscope system as well as identifying areas for future work.

1.3 Nonlinear Signal

A main advantage of multiphoton microscopy is the ability to generate label-free contrast in bulk samples. The established four nonlinear signals detected by our multiphoton microscope are two photon excited fluorescence (2PEF), second harmonic generation (SHG), three photon

excited fluorescence (3PEF), and third harmonic generation (THG) and are shown below in Figure 1.1.

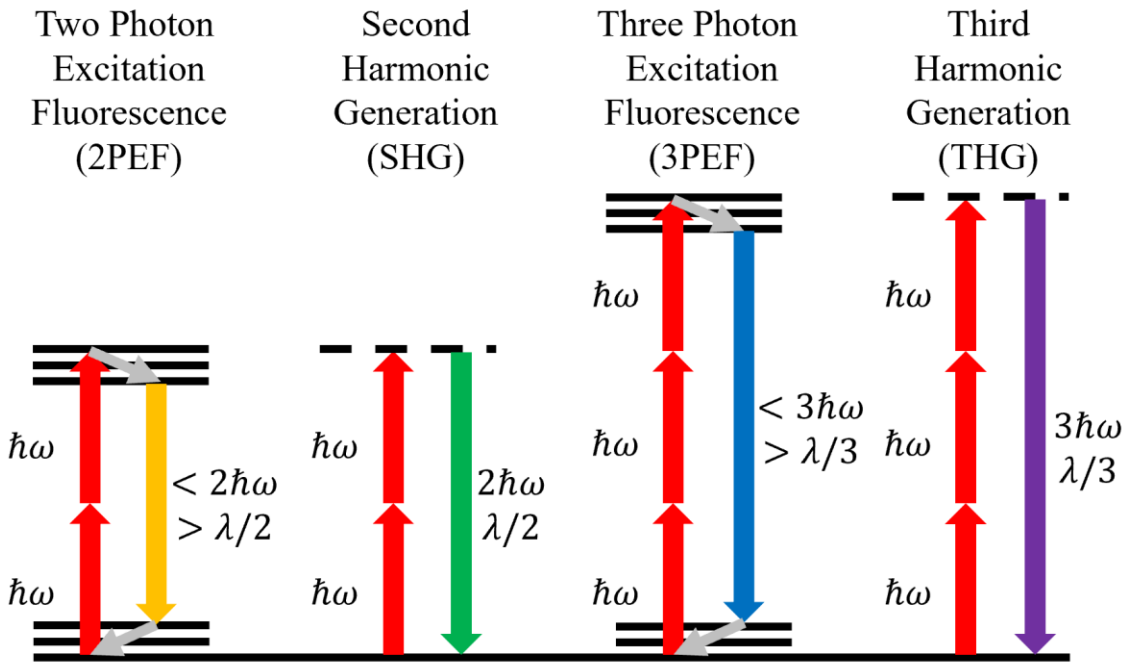

Created by Dr. Benjamin Cromey

Figure 1.1 – Energy Level Diagrams of Nonlinear Signals for Multiphoton Microscopy

Two photon excited fluorescence (2PEF) occurs when two lower energy photons are simultaneously absorbed and excite an electron to a higher energy level. The electron then loses energy as it decays and emits a photon with an energy slightly lower, and therefore with a wavelength slightly longer than the combination of the absorbed photons. This process is advantageous because it allows a longer wavelength source to excite fluorophores that would typically only be excited with a shorter wavelength source in conventional fluorescence imaging.

Second harmonic generation (SHG) occurs when two photons excite an electron to a higher virtual energy level. When the electron returns to its ground state, a photon with twice the energy and half the wavelength is emitted. SHG signal is generated in materials with a lack of centrosymmetry and is commonly used to analyze the structure of a sample.

Three photon excited fluorescence (3PEF) works similarly to 2PEF, but with three simultaneously absorbed photons. The combination of 2PEF and 3PEF allows for the excitation

of fluorophores that cover a broad range of wavelengths. With a visible source, fluorophores can be excited at wavelengths that range from the deep ultraviolet (DUV) to the visible region.

Third harmonic generation (THG) is a similar process to SHG, as it occurs when three photons excite an electron to a higher virtual state. When the electron returns to its ground state, a photon with three times the energy and one-third of the original photon wavelength is emitted. THG is very useful in multiphoton microscopy because it is generated at boundaries of changing refractive index. The ability to identify refractive index boundaries can give detailed information about the composition of a sample. Unlike SHG, which is only generated in samples with a lack of centrosymmetry, THG is generated in most samples that are imaged with an MPM.

Since all of the described nonlinear signals are dependent on the source wavelength, the wavelengths to be detected are easily calculated and a proper detection scheme can be developed. Table 1.2, below, shows the wavelengths for 2PEF, SHG, 3PEF and THG for fs pulsed fiber lasers at 1550nm, 1040nm, and 520nm.

Source Wavelength (nm)	**2PEF (nm)**	**SHG (nm)**	**3PEF (nm)**	**THG (nm)**
1550	>775	775	>517, <775	517
1040	>520	520	>347, <520	347
520	>260	260	>173, <260	173

Table 1.2 – Nonlinear Signal Wavelengths for Different Source Wavelengths

Table 1.2 shows the wavelengths to be detected and the ability of a femtosecond pulsed fiber laser to image with label-free contrast at a large range of wavelengths.

1.4 Ultrafast Fiber Lasers

When discussing lasers, “ultrafast” means having a pulse width on the order of picoseconds, femtoseconds or shorter. An ultrafast laser source utilizes short pulse lengths to

generate extremely high peak power while maintaining low average power to avoid thermally damaging a sample. Historically, ultrafast laser sources have demonstrated utility in a broad range of topics including but not limited to biology, material science, defense, metrology, and micromachining.

Titanium Sapphire (Ti-Sapphire) lasers can generate terawatts of peak power with sub 10 fs pulse durations, making them a popular choice for ultrafast laser applications, including multiphoton microscopy [13-15]. Though high performing, Ti:Sapphire lasers are bulky, expensive, and difficult to align/maintain. This opens the door to other laser technology such as the fs pulsed fiber laser. The Ultrafast Fiber Laser and Nonlinear Optics Group at the Wyant College of Optical Sciences builds lasers in an all-fiber format that utilize a ring cavity and single walled carbon nanotubes [9]. These lasers can have comparable performance to their Ti:Sapphire counterpart and are built to be handheld, cheap, and require no free space alignment.

High power fiber lasers use rare-earth doped fibers as a gain medium, allowing for a variety of source wavelengths to be produced. Ytterbium (Yb) doped gain fiber amplifies light at around 1040nm, which is a useful wavelength to image tissue due to lower water absorption. Erbium (Er) doped gain fiber can be used to amplify and generate light at around 1550nm, which is a wavelength that will travel with minimal loss through optical fiber. Thulium (Tm) and Holmium (Ho) doped fibers are used to amplify light at around 2um, which will allow for greater imaging depth [16]. To match the tunability of Ti:Sapphire lasers, fiber optical parametric oscillators (FOPOs) have been designed to amplify light at wavelengths that cannot be amplified by a doped gain fiber [17,18]. Overall, ultrafast fiber lasers offer a versatile, low cost, robust alternative to Ti:Sapphire lasers without sacrificing performance.

1.5 Multiphoton Resolution

A good microscope is designed to have the highest resolution possible so that small features may be distinguished from one another. In a typical brightfield microscope, the optical resolution is defined by the numerical aperture of the objective lens and the wavelength of the source as seen from the equation below, which was developed by Ernest Abbe in the late 19th century [19].

$$Resolution = \frac{\lambda}{2 * NA}$$

An interesting advantage to nonlinear optical microscopy is that the resolution increases due to nonlinear dependence on the electric field, which results in the narrowing of the point spread function [14]. The equations for resolution of a MPM can be seen below,

$$ResN = \frac{0.532 * \lambda}{\sqrt{N} * NA}, \qquad NA \leq 0.7$$

$$ResN = \frac{0.541 * \lambda}{\sqrt{N} * NA^{0.91}}, \qquad NA > 0.7$$

where N represents the photon process (N=2 for SHG, N=3 for THG). The following Table 1.3 shows a comparison of resolution for existing microscope systems using a 1550nm laser, a 1040nm laser, and then the proposed 520nm laser using the equations above with an assumed objective of NA=0.75.

Wavelength (nm)	Original Resolution (nm)	SHG Resolution (nm)	THG Resolution (nm)
1550	1033	770.4	629.0
1040	693.3	516.9	422.1
520	346.7	258.5	211.0

Table 1.3 – Resolution of Visible vs NIR MPMs

From Table 1.3, we can see that a MPM with a visible source of 520nm will have very high resolution due to both the lower illumination wavelength and the increased resolution associated with the nonlinear processes. While a lower wavelength source increases the resolution, it comes at the cost of depth of field, meaning that though the images will have higher resolution, the

visible MPM will not have the ability to penetrate as deep in to the sample as the existing NIR MPMs in our lab due to higher scattering losses.

1.6 Ultraviolet Microscopy

UV light is commonly used in fluorescence microscopy to image live cells. Illumination with higher energy photons is advantageous because the photons can excite lots of fluorophores that cannot be seen when using a visible or NIR source. Caution must be used with lower wavelengths as UV light is known to induce cellular damage under the right exposure conditions [20]. In brightfield microscopy, the risk of damage is higher due to the long exposure time and large area exposed. Laser scanning microscopy offers a better solution to minimize photobleaching. In confocal microscopy, a form of laser scanning microscopy, only light from the focal plane is detected, however this is due to the use of a pinhole to filter out background signal. The background signal, though not detected, can cause additional excitation in a sample, and therefore has an increased chance to cause damage. Multiphoton microscopy, on the other hand, only generates signal in the focal volume of the objective, which leads to a very small portion of the sample being illuminated before the laser continues to scan to the next point. This means that the UV light is only focused on a small area for a short period of time and there are no additional parts of the sample unnecessarily exposed to the high energy photons. Therefore, the chance of photobleaching is reduced compared to brightfield microscopy and even other forms of laser scanning microscopy.

Extensive work has been done in UV microscopy to examine the excitation and emission of different fluorophores, some of which is summarized in Table 1.4 below [21-26]. In theory, all of the samples/materials listed in Table 1.4 will be excitable with a visible femtosecond pulsed source. From a biological perspective, this will be very advantageous in the imaging of amino acids, neurotransmitters, serotonin, and dopamine. Knowledge of different neurotransmitter interactions could lead to a better understanding of bodily functions and regulations such as sleep, memory, and metabolism [21]. Fluorescence of the sensory receptors in human dentine can give valuable insight into the innervation of teeth, while imaging human skin with UV light can give information on aging, certain forms of cancer, acne, and more [22,23]. The advantages to UV microscopy in the biological sciences extends past human samples. Fluorescence in plants

allows for monitoring of stresses caused by biochemical and physiological factors which can impact the rate and efficiency of photosynthesis [24]. In the field of material science, UV excitation has been used to create tunable, near-ultraviolet, coherent sources by optically pumping Ce^{+3} ions in $LiYF_4$ [25]. Additionally, the UV spectroscopic properties of coal pyrolysis tars give information about coal rank, composition, and pyrolysis conditions [25,26].

Sample/Material	**Excitation (nm)**	**Emission (nm)**	**Reference**	**Year**
Amino Acids	200-300	260-440	Teale and Weber, Biochem J. Vol 65, p476	1956
Human Dentine	250-380	250-380	Archs oral Biol. Vol25 p641	1980
Human Skin	290-420	340-600	Vibrational Spectroscopy 28 pp17–23	2001
Leaves, plants	200 - 400	400-630	J. Planet Physiol. Vol148 p536, Env. Exp. Botany Vol 73, p3 Agronomie 19, p543 Marine Chem. 62 p 137 Opt.Exp. Vol 12, p4457	1996 2011 1999 1998 2004
Rare Earth	100-200	250-450	Phys. Rev. B, Vol. 8, 4989	1973
Coal Pyrolysis Tars	200-300	300-540	Energy, fuels, Vol. 8, No5	1994

Credit to Orkhongua Batjargal for her work in this research.

Table 1.4 – Excitation and Emission of Various Materials Using UV Light [21-26]

Table 1.4 shows only a few of the many new types of samples that can be illuminated and analyzed with a visible multiphoton system.

1.7 Current Multiphoton Microscope Technology

As mentioned previously, NIR multiphoton microscopes are designed and built in lab using off the shelf components from Thorlabs and a LabView code written by Dr. Soroush Mehravar and improved by Dr. Shai Vardeny. Different reflective and refractive systems have

been constructed and are detailed in the literature [7,8]. Reflective systems have the advantage of eliminating chromatic aberrations and enabling the use of different wavelength sources, while refractive systems have the benefit of easier alignment with the use of cage systems. Figure 1.5 below shows the schematic of a current refractive MPM used in lab.

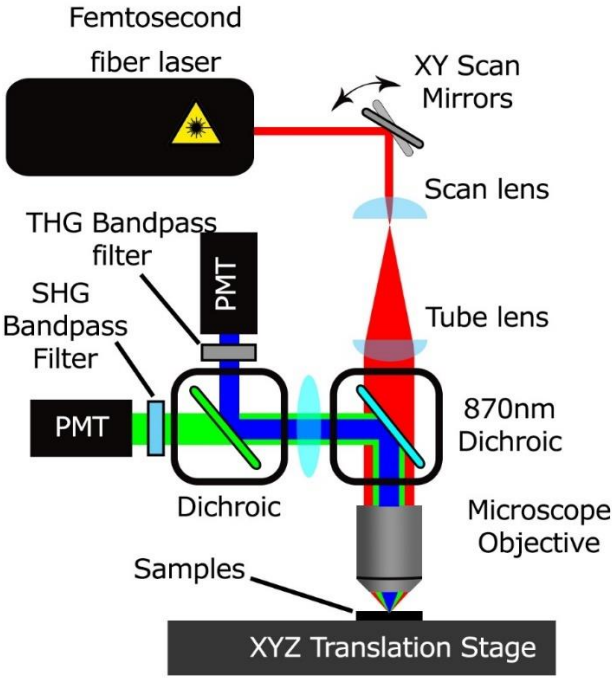

Created by Dr. Benjamin Cromey

Figure 1.5 – NIR Multiphoton Microscope Schematic

The layout of an example MPM is seen above. The source, a NIR femtosecond pulsed fiber laser is collimated and raster scanned in a point by point manner across the sample by a pair of galvo mirrors. The beam is then sent to a scan and tube lens that work as a 4x telescope to expand the beam so that it fills the back aperture of the microscope objective. The longer wavelength source (1040nm or 1550nm) transmits through an 870nm dichroic and is focused on the sample. The nonlinear signal is generated in the volume of the focal plane and a translation stage allows the location of the focal plane to be changed. The nonlinear signal is then collected through the objective in an epi-detection setup. Since the nonlinear signal will be a second or third harmonic of the original source wavelength, it will be short enough to reflect off the 870nm dichroic. The reflection from the dichroic sends the light to another dichroic mirror and bandpass filters that control what wavelength will reach the two PMTs. The layout in Figure 1.5 is

effective for a NIR source which detects nonlinear signal in the visible, but it is not ideal for UV light detection. A high-quality objective that works well for the visible/NIR wavelengths will not transmit light for UV epi-detection. An alternative is to use a UV objective which would transmit the visible source and UV light for epi-detection, but that comes with reduced image quality due to the limited glass types that effectively transmit UV light. The solution is a transmission detection system with a high-quality visible objective to transmit the source wavelength to the sample and then a high-NA UV objective to collect the signal. The design of the microscope illumination and detection system will be further detailed in Chapter 3.

2. Laser Description and Characterization

The development of an ultrafast visible fiber laser source is not trivial since there is no gain fiber that will emit amplified light in the visible spectrum. The concept behind this visible laser is to use a Ytterbium (Yb) amplifier to amplify light at 1040nm. The 1040nm output is then compressed, frequency doubled with a nonlinear crystal, and the SHG from that crystal at 520nm will be used as the source for the microscope. Other visible MPMs in the literature use a Ti:Sapphire laser, an OPO, and a nonlinear crystal to generate visible light. Even though there are free space components that require careful alignment, the fiber format of this laser leads to a cheaper, easier to align, and more compact visible fs pulsed laser.

The laser schematic can be seen below in Figure 2.1 and is broken up in to three parts, the pre-amplifier, main amplifier, and free space components. Each part of the laser system will be fully discussed in the following sections.

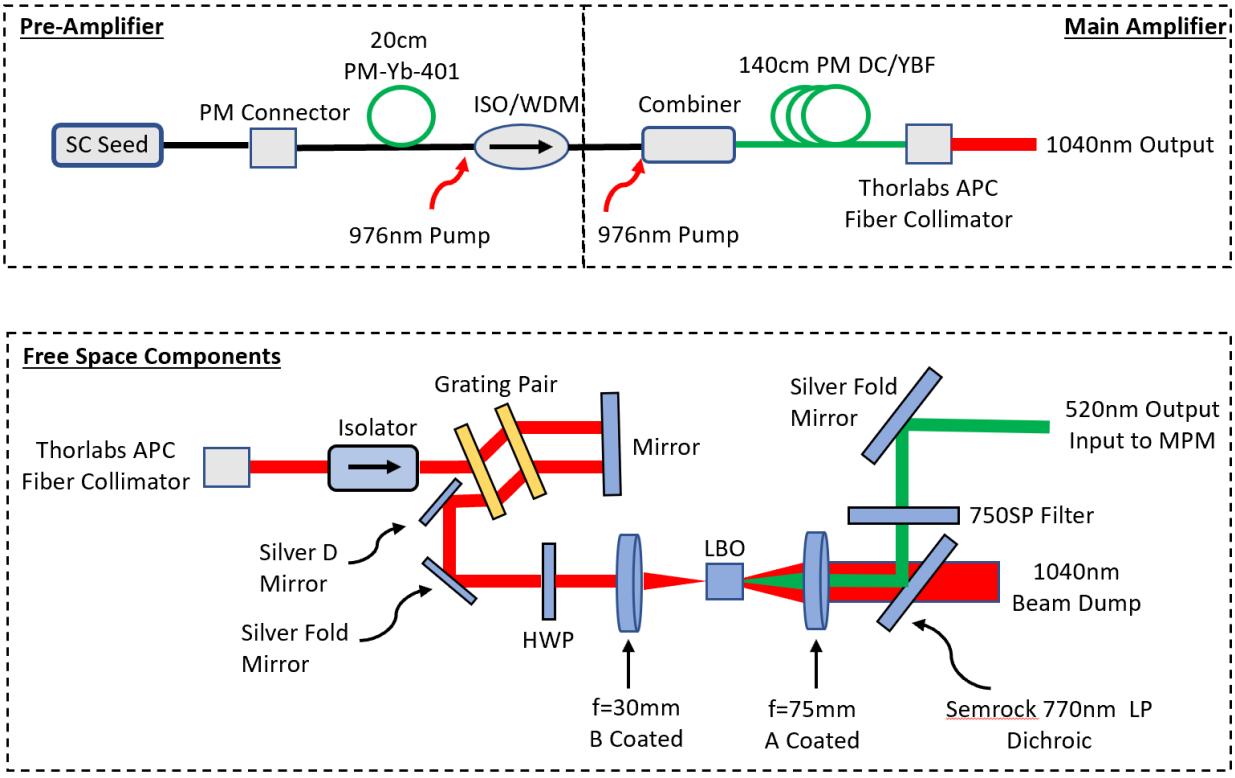

Figure 2.1 – (Top Left) - Fiber laser components that make up the pre-amplifier. (Top Right) – The main amplifier

(Bottom) Free space components used to frequency double the amplified 1040nm light

2.1 Pre-Amplifier Design and Characterization

The purpose of the pre-amplifier is to amplify the 1040nm portion of a supercontinuum oscillator. The 1040nm signal will then be further amplified such that there is sufficient power for multiphoton microscopy. Figure 2.2, below, shows the schematic of just the pre-amplifier section from Figure 2.1.

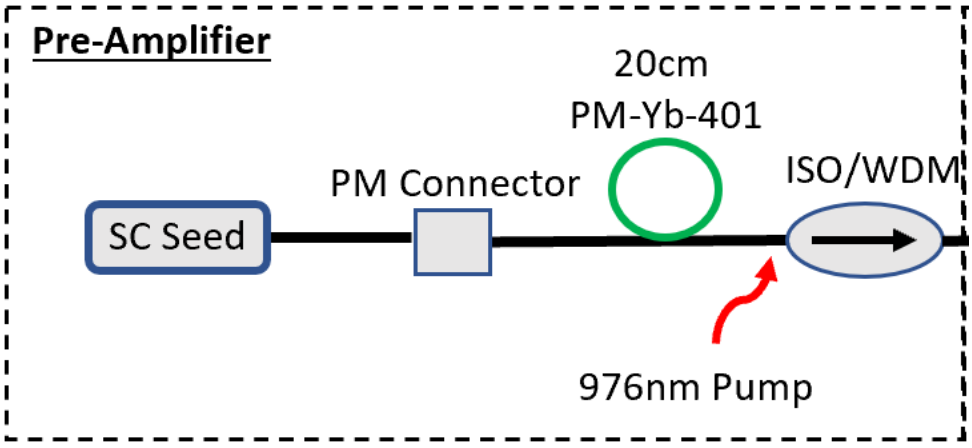

Figure 2.2 – Fiber Pre-Amplifier

On the far left of Figure 2.2, the "SC Seed" represents the supercontinuum oscillator that will act as the seed for the pre-amplifier. The loaner oscillator, manufactured by KPhotonics, has a very broad spectrum, an average power of 3.2mW, a 50MHz repetition rate, and pulse width of one picosecond. Figure 2.3, below, shows the characterization of the supercontinuum oscillator.

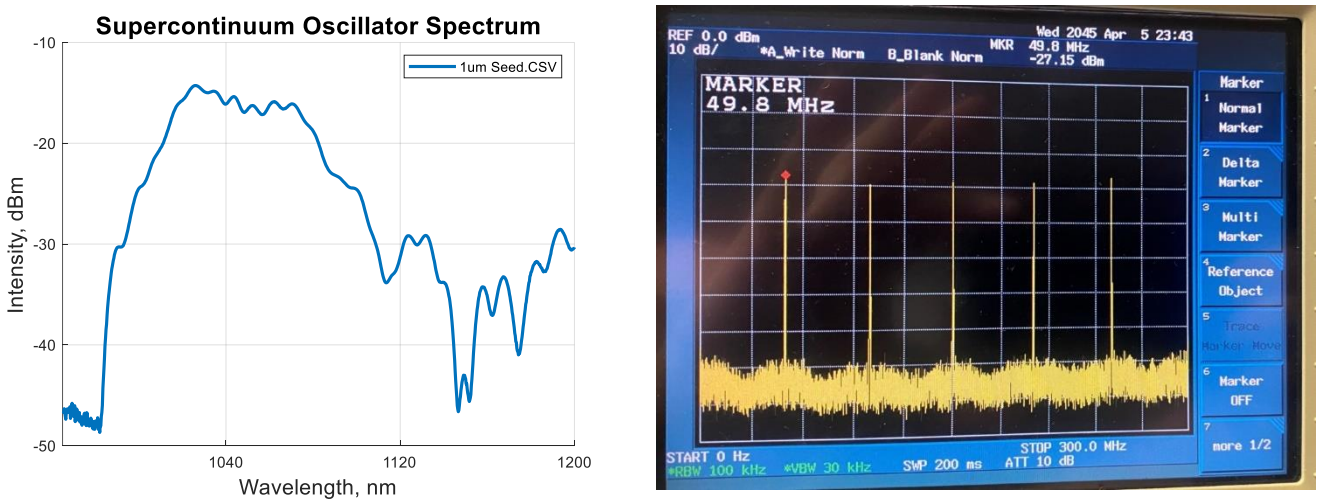

Figure 2.3 – Characterization of Supercontinuum Oscillator, (Left) – Spectrum, (Right) – Repetition Rate

The spectrum from Figure 2.3 (left) was taken with an Agilent 86140B Optical Spectrum Analyzer (OSA) and shows the broad spectrum associated with a supercontinuum source. The goal of the rest of the pre-amplifier system is to further amplify the portion of the spectrum centered around 1040nm. The repetition rate of the oscillator was also determined to be 50MHz as seen from the image of the RF Spectrum Analyzer in Figure 2.3 (right).

Since polarization is critical in the process of frequency doubling light with a nonlinear crystal, the highly polarized supercontinuum seed output was coupled back into PM 980 Panda fiber with the use of a connector. The connector places the two fiber ferrules close to one another without the need for alignment to maximize transmission and ensure polarization alignment between the two fibers. After the connector, there is 45cm of PM 980 Panda fiber, followed by 20cm PM-Yb-401 gain fiber. The gain fiber is then spliced to 45cm PM 980 Panda fiber that connects to one input of a Lightel 980/1040nm Isolator/Wavelength Division Multiplexor (WDM) Hybrid. Connected to the other input of the Isolator/WDM is a pump diode from Wavelength Electronics LDTC1020 that emits at 976nm. The pump laser will act to core-pump the PM-Yb-401 such that the Yb atoms in the gain fiber absorb the 976nm pump and amplify at 1040nm. The WDM aspect of the ISO/WDM allows the pump light to enter the core of the PM-Yb-401 fiber and amplify the 1040nm signal, while the isolator aspect effectively blocks any

residual, unabsorbed pump light and ensures blocking of backward propagating light. Figure 2.4 below shows the characterization of the pump laser diode that is spliced to one input of the isolator/WDM.

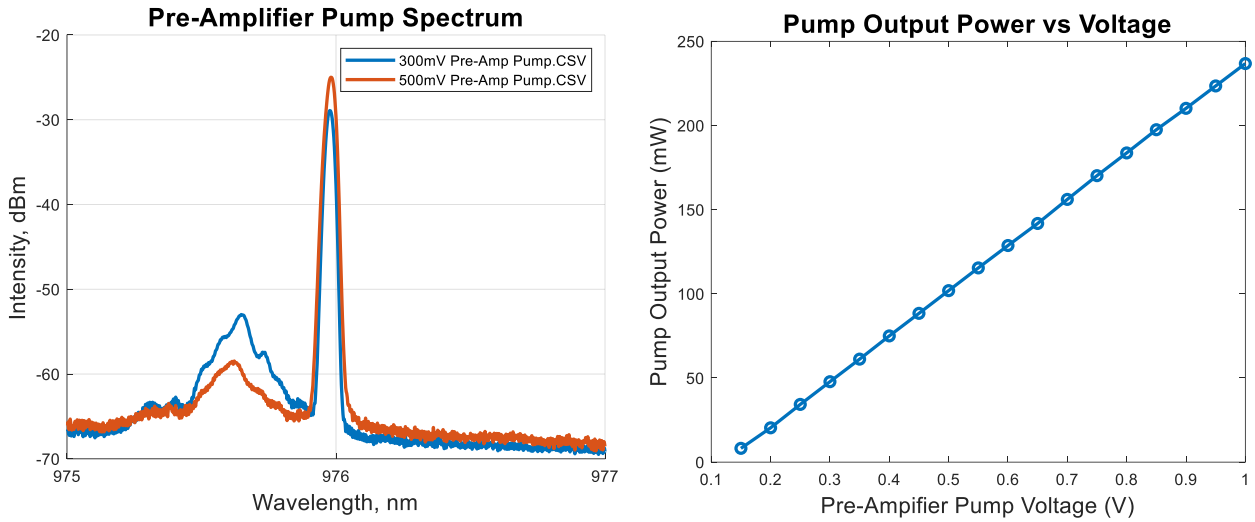

Figure 2.4 – Characterization of Pre-Amplifier Pump Laser Diode, (Left) – Spectrum centered at 976nm, (Right) – Output pump power as a function of pump voltage.

The pre-amplifier pump spectrum can be seen on the left side of Figure 2.4. It has a narrow peak at 976nm which is the correct wavelength for exciting Yb atoms in the doped gain fiber. From the right plot of Figure 2.4, the adjustable voltage on the pump diode controls the pump current and thus the output optical power from the pump laser. A pump voltage that is too low will not properly saturate the pre-amplifier, and can lead to low laser power and other undesirable effects such as amplified stimulated emission (ASE). The output of the ISO/WDM is the amplified 1040nm signal and is characterized below in Figure 2.5

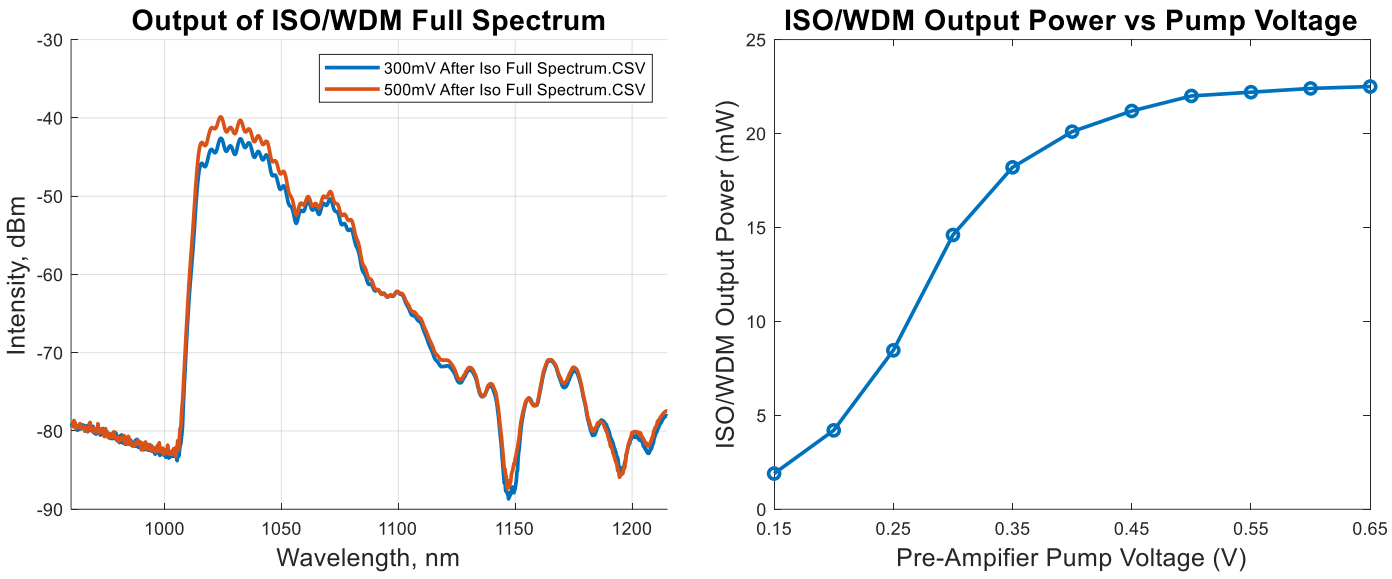

Figure 2.5 – Characterization of the output of the ISO/WDM. (Left) – Pre-amplified spectrum. (Right) – Isolator output versus pump voltage showing saturation

In Figure 2.5, above, the left plot shows the characterization of the laser output after the ISO/WDM. The spectrum is slightly narrower than what was previously seen from the supercontinuum oscillator, which is due to the gain experienced by the 1040nm light. The spectrum also shows that there is no residual pump light at 976nm due to absorption in the gain fiber. The right plot shows the saturation of the pre-amplifier. Compared to the laser power vs voltage plot in Figure 2.4, the ISO/WDM output power vs pump voltage plot plateaus towards the higher voltage. From the plot on the right in Figure 2.5, it was determined that running the pre-amplifier pump at 0.550V (corresponding to 0.275 A pump current) was appropriate to saturate the PM-Yb-401 gain fiber.

2.2 Main Amplifier Design and Characterization

The purpose of the main amplifier is to further amplify the 1040nm portion of the output of the ISO/WDM. This is done similarly to the design of the pre-amplifier and the schematic can be seen below in Figure 2.6.

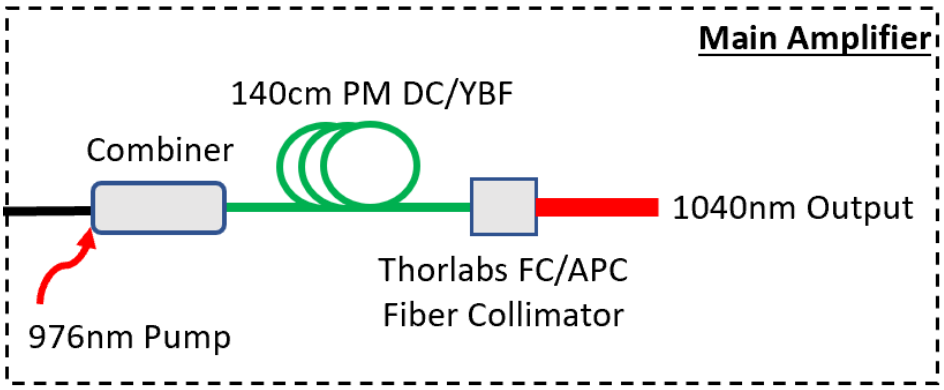

Figure 2.6 – Schematic of the main amplifier

The black fiber entering the combiner from the left in Figure 2.6 is PM 980 Panda fiber from the ISO/WDM output spliced in to 10cm of Nufern PM 10/125 DCF 0.08/0.46NA gain fiber that connects to the combiner. The other input to the combiner is a 105um core fiber from a BWT Beijing K976S02RN-3.000W pump laser diode spliced to Nufern 105/125 0.22NA fiber. The combiner (OPNETI H26360201 multimode pump and PM signal combiner) output acts as the start of a double clad Yb gain fiber amplifier. This works by allowing the previously amplified 1040nm signal to travel through the core of the gain fiber, while the pump light travels via TIR at the cladding. Double clad amplifiers are popular in high power fiber laser applications and can have very high efficiency. The output combiner fiber is 45cm of Nufern PM 10/125 DCF 0.08/0.46NA fiber followed by 95cm of additional Lekkiki PM-Dc-Yb fiber to further amplify the 1040nm signal. After splicing the Nufern and Lekkiki DC (double clad) fibers together, the outside of the splice was recoated to protect the splice and keep the pump light confined in the cladding. At the output of the main fiber amplifier is a PM connector that has the rods of the PM fiber aligned with the key of the connector. This alignment was done with a Thorlabs ERM100 Extinction Ratio Meter. Due to tight tolerances of the connector, and perhaps a mislabeled fiber diameter, the fiber tip was submersed in Armor Etch, a sodium bifluoride based glass etchant for two minutes to allow the fiber tip to fit through the connector ferrule before being secured with epoxy. To collimate the output from the ferrule, a Thorlabs F220-APC-1064 fiber collimator is attached to the connector and secured in a tip/tilt mount for alignment.

Like the pre-amplifier pump, the main amplifier pump was characterized to verify the spectrum and output power. The result is shown below in Figure 2.7.

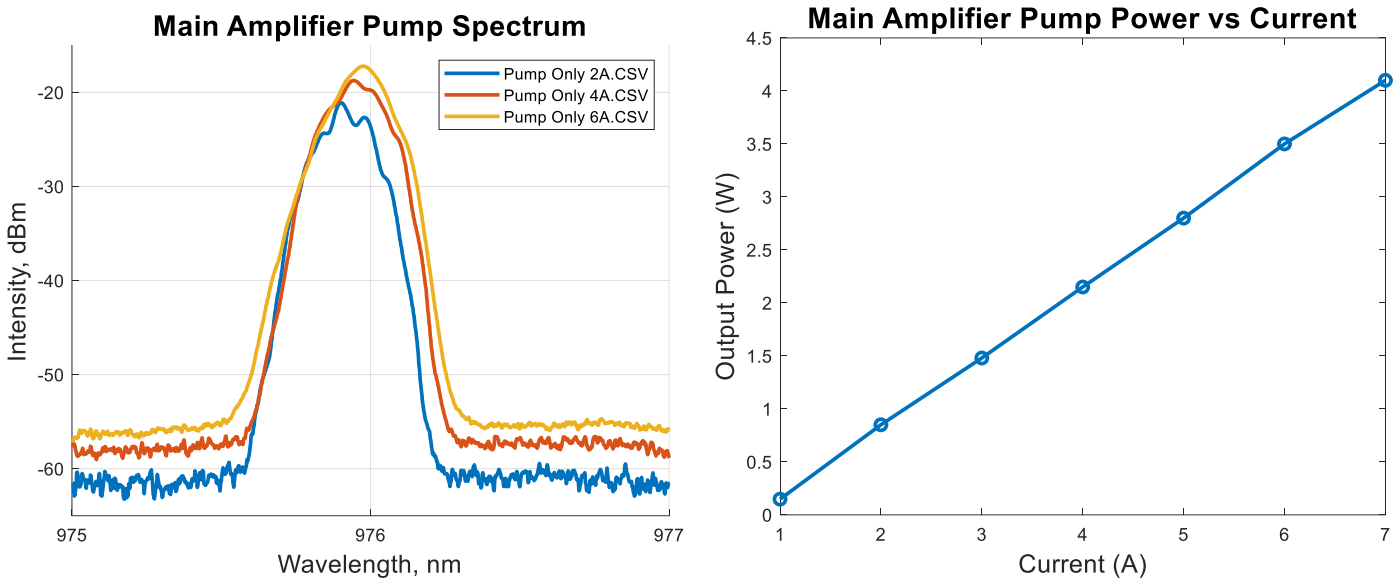

Figure 2.7 – Characterization of the main pump laser. (Left) – The spectrum showing emittance at 976nm. (Right) – Power out of the Pump Laser vs Driver Current

Figure 2.7 shows that the main amplifier pump emits at a wavelength of 976nm and is much more powerful than the pre-amplifier pump. The laser power was characterized up to 7A, though the pump can run up to 9A. The high powered 976nm pump through 140cm of Yb gain fiber effectively amplifies light at around 1040nm. The performance of the entire system after the output of a fiber collimator is characterized below in Figure 2.8.

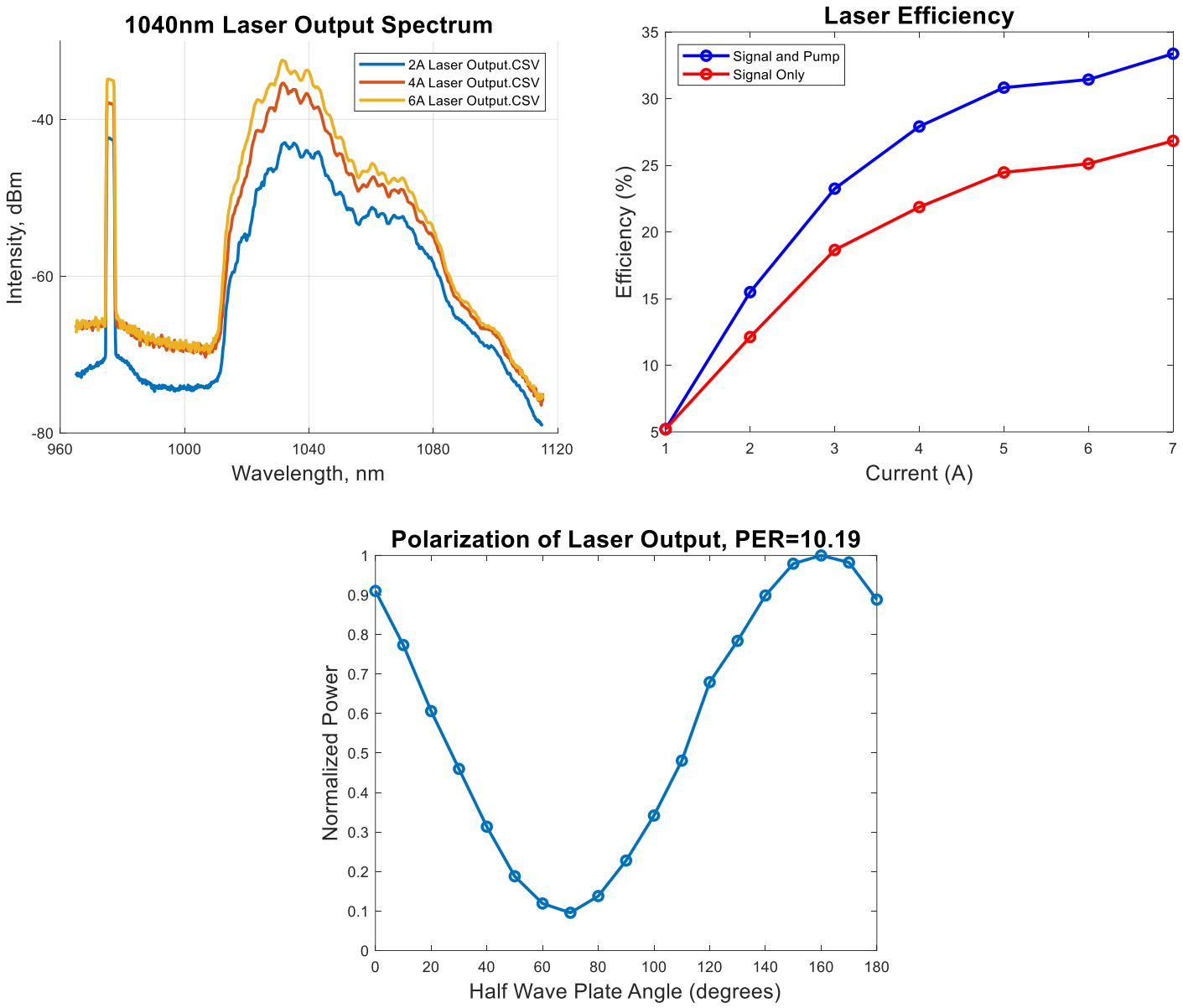

Figure 2.8 – Characterization of 1040nm laser output. (Top Left) – Spectrum at the laser output. (Top Right) – Efficiency of laser power vs pump power. (Bottom) – Polarization extinction ratio showing the polarized output.

Figure 2.8 shows the characterization of the amplified 1040nm laser spectrum, efficiency, and polarization. The spectrum shows the amplified signal around 1040nm for different pump currents. There is a large peak at 976nm, which is from unabsorbed pump light through the gain fiber. This unabsorbed pump causes lower efficiency, since it is all pump light that was not

converted to 1040nm light in the gain fiber. 140cm of gain fiber should be sufficient, but perhaps adding more gain fiber to the system would increase the performance. This could be an area of future work if higher laser power is desired. The efficiency plot on the top right shows that the laser system has around 25% efficiency of converting pump light into the 1040nm signal. For this plot, the remaining pump light was blocked with the use of an iris aperture and the signal power itself for was measured. Lastly, the bottom plot shows the polarization of the 1040nm output to verify that each polarization maintaining (PM) splice was done correctly. A highly polarized output beam is very important since the polarization state will greatly impact the transmission through the free space isolator and the green light power generated from the nonlinear crystal. The polarization extinction ratio (PER) was plotted using a half wave plate, a linear polarizer, and power meter. The PER of the laser output was around 10.5, with the largest PER drop occurring at the combiner. Even though the laser could have improved efficiency, there is more than enough 1040nm signal needed to generate green light from the crystal.

2.3 Free Space Components and Green Light Generation

Although it is beneficial to build the laser in an all-fiber format, some free space components are necessary to compress the 1040nm pulse and frequency double it through the crystal. The schematic of the free space components is shown below in Figure 2.9.

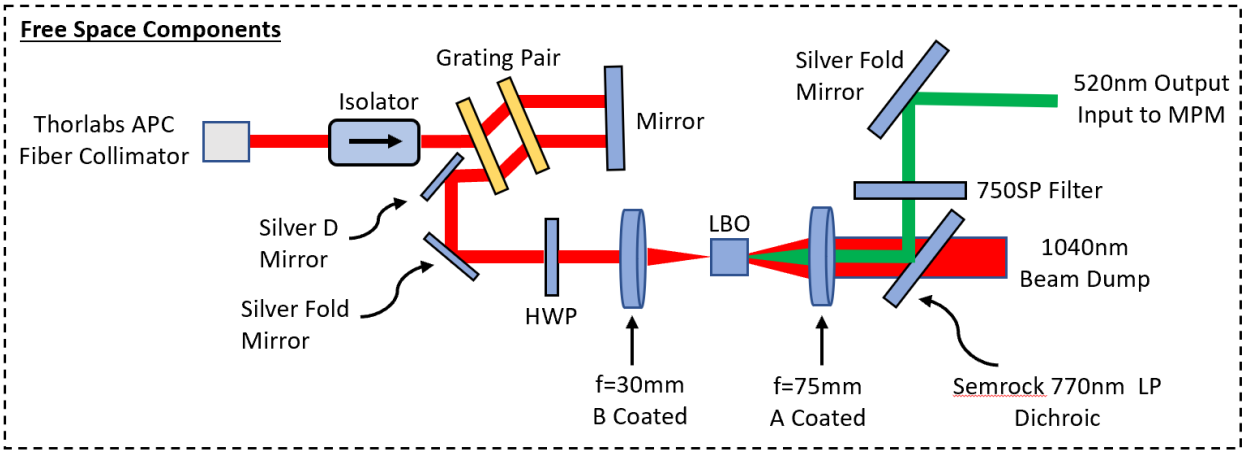

Figure 2.9 – The free space components used for green light generation

The start of the free space components is the collimated 1040nm laser output that was characterized in Figure 2.8. Going through the diagram above, the collimated light is first sent through a free space isolator. The isolator allows light in only one direction, so harmful, high-powered back reflections to the fiber collimator are eliminated. The isolator also produces a purely polarized output due to TIR and beam splitting prisms oriented at Brewster's angle which will only transmit p-polarized light. The fiber collimator was rotated by hand in the tip/tilt mount to maximize the transmittance through the isolator. Due to the laser output PER of around 10.5 from Figure 2.8, almost 80% of the light was transmitted through the isolator. Next, the light travels to a grating pair compressor. The grating pair compressor has a basic function to add anomalous dispersion that cancels out the dispersion induced on the light traveling through fiber. This acts to compress the pulse in time based on the grating pair distance. After transmitting and diffracting through the grating pair, the light reflects off a one inch, slightly tilted silver mirror and travels back through the grating pair effectively doubling the amount of anomalous dispersion. A silver pickoff (D) mirror with a sharp edge is used to separate the incoming from the closely separated reflected beam. The compressed pulse reflects off the pickoff mirror, and then reflects off a silver fold mirror oriented at 45 degrees to send the light back towards the microscope and the crystal. A HWP is inserted in the beam path for precise control over the beam polarization state. The beam is then focused through the crystal by a Thorlabs AC254-030-ML B-coated f=30mm achromatic doublet and recollimated by a Thorlabs A-coated 75mm convex-plano lens. The lens pair acts to magnify the beam to around 4mm which is the appropriate size entering the microscope. The output, which is a mix of the generated green light and the residual laser light, is sent to a Semrock 770nm dichroic mirror which transmits the residual 1040nm laser light to a beam dump and reflects the 520nm signal upwards towards another silver fold mirror that will send the green light to the microscope. In the beam path there is one other Semrock 750SP filter to ensure that all 1040nm light is filtered out of the microscope input beam.

2.3.1 Grating Pair Compressor

The grating pair compressor was introduced in the previous section and serves the very important role of compressing the pulse in the laser system. In multiphoton microscopy, a short pulse on the order of 100fs is desirable so that the peak power is high to observe nonlinear

effects, but the average power is low to avoid burning a sample. The grating pair is necessary in this setup due to the positive dispersion from the silica optical fiber. The fiber induces some group delay dispersion (GDD) which is the temporal delay between different spectral components of an ultrashort laser pulse [27]. In this setup, the grating pair induces negative dispersion due to the different optical path lengths traveled by the different spectral components of the pulse. This essentially allows the shorter wavelengths to "catch up" to the longer wavelengths in time. The setup of the gratings is shown below in Figure 2.10.

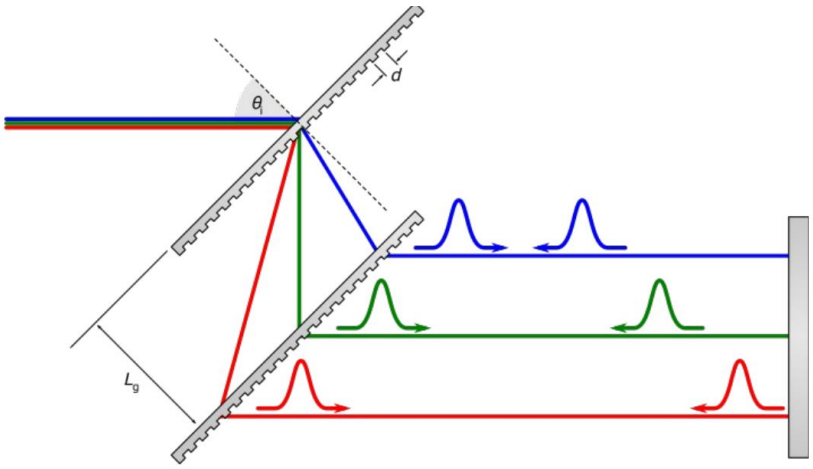

Figure 2.10 – Grating pair compressor in the Treacy configuration [27]

Figure 2.10 shows the Treacy grating configuration used in this laser setup. A mirror is used to retroreflect the beam back through the gratings, which doubles the negative dispersion and restores the spatial coherence of the beam. The gratings used were transmissive gratings with 1000 line pairs per millimeter (lp/mm). They were oriented parallel to one another, but at an angle of 31 degrees to the optical axis to maximize the diffraction efficiency. The first grating was secured to the optical table while the second grating and mirror for retroreflection were mounted together on a translation stage so the pulse could be compressed simply translating the stage, which adjusts the grating spacing. The actual grating pair setup can be seen below in Figure 2.11.

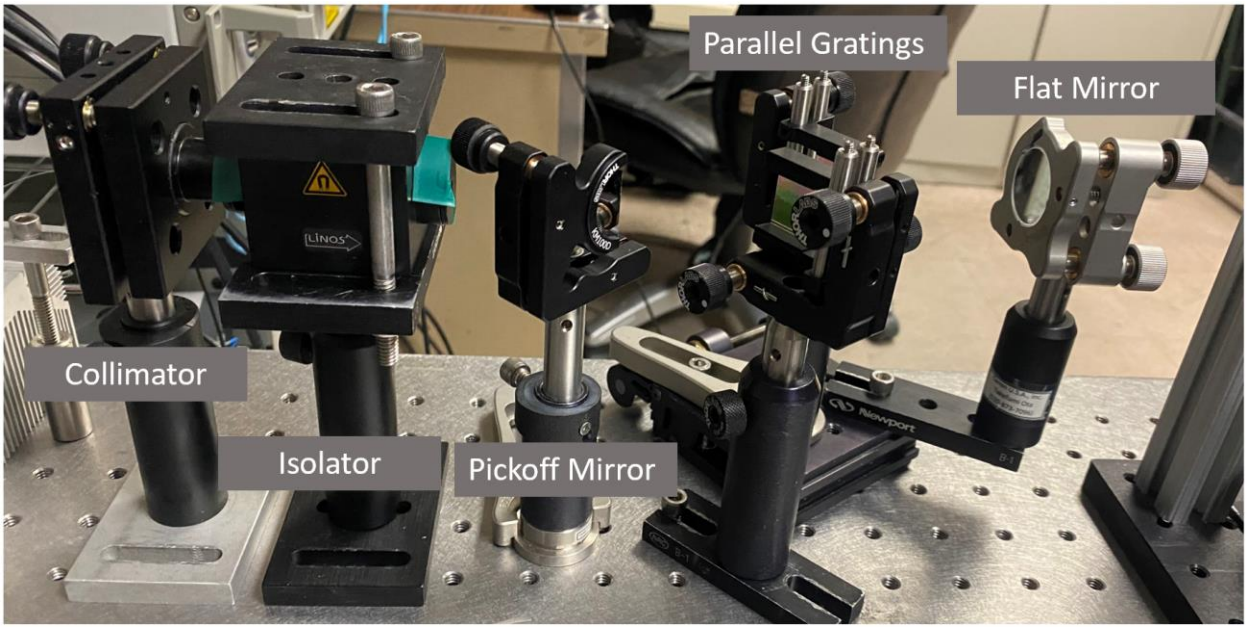

Figure 2.11 – Treacy grating pair compressor setup

From Figure 2.11, simply adjusting the translation stage to change the distance between the two gratings and adjusting the tip/tilt of the flat mirror will compress the returning pulse and slightly displace it from the original pulse such that the pickoff mirror can separate the two beams. Theoretically, the GDD from the fiber laser due to the fiber length is demonstrated by the following equation [27].

$$\frac{d^2\phi}{d\omega^2} = \frac{\lambda^3 L_d}{2\pi c^2}\frac{d^2n}{d\lambda^2} \qquad [2.1]$$

Where $\frac{d^2\phi}{d\omega^2}$ represents the GDD, L_d is the length of the optical fiber, λ represents the wavelength, c is the speed of light, and $\frac{d^2n}{d\lambda^2}$ is the second derivative of the index of refraction with respect to wavelength. The quantity $\frac{d^2n}{d\lambda^2}$ can be found by taking the second derivative of the Sellmeier equation for SiO2, shown below.

$$n^2 - 1 = \frac{0.6961663\lambda^2}{\lambda^2 - 0.0684043^2} + \frac{0.4079426\lambda^2}{\lambda^2 - 0.1162414^2} + \frac{0.8974794\lambda^2}{\lambda^2 - 9.896161^2} \qquad [2.2]$$

Equation 2.2 shows the Sellmeier equation for SiO2 and the second derivative with respect to wavelength was calculated with Mathematica. Using a measured total fiber length of three meters, Equations 2.1 and 2.2 give a GDD of 0.0546 ps^2. The GDD from the gratings at the appropriate spacing must induce value of around -0.0546 ps^2 to optimally compress the pulse. The equation for GDD of a grating pair compressor is seen in Equation 3.3.

$$\frac{d^2\phi}{d\omega^2} = -\frac{m^2\lambda^3 L_g}{2\pi c^2 \Lambda^2}\left[1-(-m\frac{\lambda}{\Lambda}-sin\theta_i)^2\right]^{-3/2} \quad [2.3]$$

Where m is the diffraction order, Lg is the grating separation, Λ is the grating period, and θ_i is the angle of incidence on the first grating. With the aid of an online calculator at https://www.lasercalculator.com/grating-pair-dispersion-calculator/, the calculated distance between the gratings was around 0.5cm when taking into account the double pass configuration. This is assumed to be an underestimate since only fiber length after the oscillator in the signal path was measured. There is unaccounted for fiber from the oscillator, other fiber components, and glass in the initial free space components that contribute additional positive dispersion that would cause the grating pair separation to increase.

The pulse width was then measured using a Femtochrome FR-103MN autocorrelator and an oscilloscope. Once the autocorrelator was properly aligned and signal was seen on the oscilloscope, a calibration was performed to convert a time reading on the oscilloscope to a pulse width in femtoseconds. This is done by translating a retroreflector by a known distance in millimeters from a micrometer reading. The shift in the pulse on the oscilloscope will then move accordingly. Using the speed of light, a relation between the time on the oscilloscope and the

actual time can be determined. My calibration had a result of 30.573 ps in real time / ms on the oscilloscope. The results of the autocorrelation measurement are shown below in Figure 2.12.

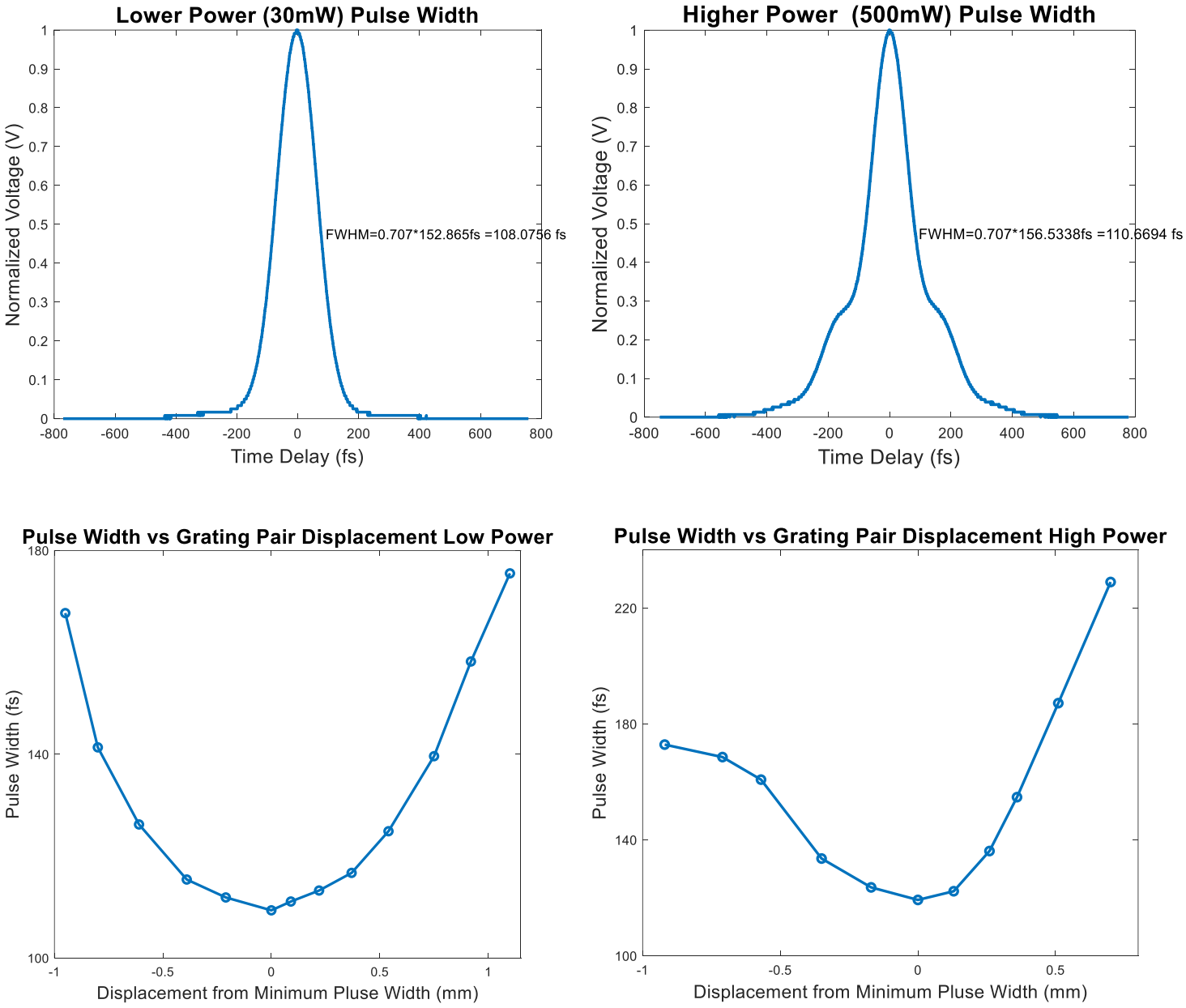

Figure 2.12 – Results from autocorrelation measurement for pulse width. (Top Left) – Pulse width at 30mW laser power. (Bottom Left) – Pulse width vs grating pair separation at 30mW laser power. (Top Right) – Pulse width at 500mW laser power. (Bottom Right) – Pulse width vs grating pair separation at 500mW laser power.

From the top row of Figure 2.12, the pulse compression with the grating pair gave a pulse with of 109fs for the 30mW laser and 111fs for 500mW laser power. These are the pulse widths at the full width half max (FWHM) of the plots above. The measured value from the oscilloscope using the previously described calibration factor is displayed. That value is then multiplied by 0.707 which is the deconvolution factor for an assumed Gaussian pulse. The bottom row of Figure 2.12 verifies that the grating separation was for minimum pulse width. Using a caliper, a grating separation of 2.195cm was optimal for the lower power pulse and a separation of 2.12cm was optimal for the higher power pulse. With this compressed pulse, the average power, rep rate, pulse energy, and peak power can be calculated for the 1040nm laser.

$$Pulse\ Energy = \frac{Average\ Power}{Repition\ Rate} = \frac{500mW}{50MHz} = 10nJ$$

$$Peak\ Power = \frac{Pulse\ Energy}{Pulse\ Width} = \frac{10nJ}{111fs} = 90kW$$

Average Power	Repetition Rate	Pulse Energy	Peak Power
500mW	50MHz	10nJ	90kW

Table 2.13 – The specifications of the laser output after grating pair compression.

From the top right of Figure 2.12, there are tails on each side of the Gaussian pulse. This represents nonlinear effects at higher laser power. The spectrum of the 1040nm laser was taken once more at the grating pair output with the compressed pulse to see if there were any observable nonlinear effects.

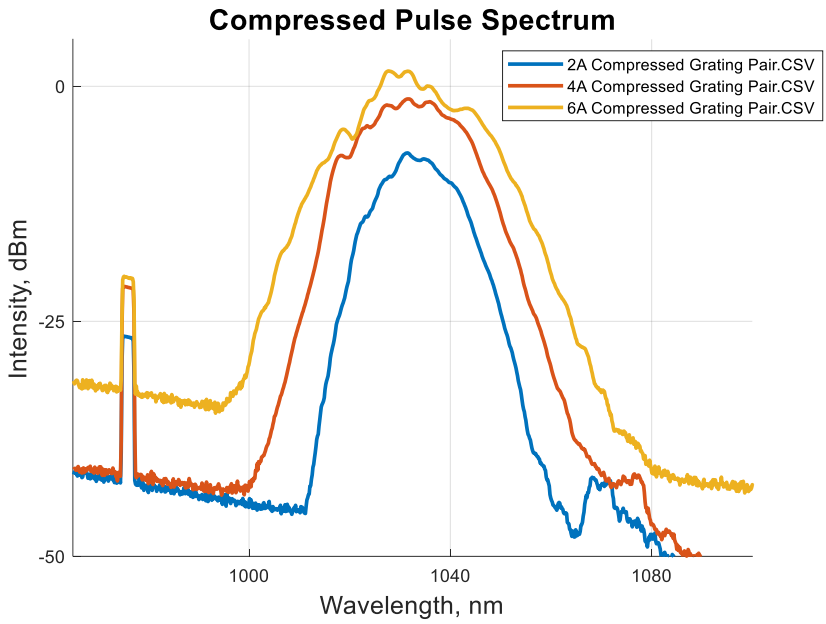

Figure 2.14 – Spectrum after pulse compression

From Figure 2.14, we see the spectrum after the pulse compression by the grating pair. There is a peak at around 1040nm and the 976nm pump light is gradually filtered out due to the optical components being designed at 1040nm and not 976nm.

The compression of the pulse to around 110 fs with the grating pair is a promising result, as the shorter pulses will be advantageous for multiphoton microscopy as well as maximizing the amount of green light obtained from frequency doubling the source through the nonlinear crystal.

2.3.2 Frequency Doubling with the Crystal

Now that the laser pulse is properly compressed, the light can be frequency doubled through the nonlinear crystal. This is not a trivial task, as the proper crystal must be chosen based on factors such as efficiency, damage threshold, and pulse broadening. The crystal was purchased previously by Orkhongua Batjargal, and her research and simulation results are presented below. First, the damage threshold of the various crystals will be analyzed. The peak irradiance from the 1040nm beam, from Table 2.13 is calculated below.

$$Peak\ Irradiance = \frac{Peak\ Power}{Focused\ Beam\ Size} = 3.6 GW/cm^2$$

Where the focused beam size can be determined by using the Gaussian beam equations and an assumed focal length (f) of 30mm for the focusing lens.

$$Focused\ Beam\ Size\ (W_1) = \frac{\lambda f}{\pi \omega_o} = 0.015mm$$

Where ω_o, the initial beam size was measured to be 1.7mm. Based on the calculation for peak irradiance above, it is imperative that the crystal not be damaged by 3.6GW/ cm^2.

Table 2.15, below, shows the different damage thresholds for different crystal types.

Crystal	**Wavelength (um)**	**Pulse Duration (ns)**	**Damage Threshold (GW/ cm^2)**
LBO	1	1	45 [29,30]
		0.1	25 [28]
		0.01	>3.3 [31]
	0.5	1	26 [29,30]
		0.1	4.5 [31]
		0.01	4.1 [31]
BBO	1	10	2.6 [32]
		0.1	15.6 [28]
	0.5	10	>1 [32]
	0.25	10	0.15 [32]

Research done by Orkhongua Batjargal

Table 2.15 – Damage threshold of LBO and BBO crystals

From Table 2.15 above, the LBO crystal has a higher damage threshold and is more suitable for this application than a BBO crystal.

The next factor to analyze is the efficiency of the different crystals, as an inefficient crystal would cause too low power of green light for multiphoton microscopy. This was done using SNLO software to simulate second harmonic generation in the crystals. The simulation results are as follows in Table 2.16 with an assumed 30nJ, 100fs 1040nm pump pulse.

Crystal	Length (mm)	Efficiency (%)
BIBO	1	29.4
	1.5	39.6
	2	46.6
BBO	1	18.8
	2	33
	3	40.3
LBO	3	26.7
	4	34
	5	40

Simulation and Results done by Orkhongua Batjargal

Table 2.16 – Efficiency results for different crystals and lengths

Table 2.16 shows the different theoretical efficiencies for converting 1040nm light into 520nm light. Based on the relatively high efficiency, reasonable cost, and high damage threshold, a NewLight Photonics 4x4x4 LBO Crystal was selected.

Next, the proper focusing lens to maximize the second harmonic generation was chosen. The optimal lens would have a confocal parameter, or depth of focus, equal to the length of the crystal (4mm). This will allow the beam to be focused over the entire length of the crystal and maximize signal generated. To determine the proper focal length, the following Gaussian beam equations were used.

$$Focused\ Beam\ Size\ (W_1) = \frac{\lambda f}{\pi \omega_o}$$

$$Rayleigh\ Range\ (ZR) = \frac{\pi {W_1}^2}{\lambda}$$

$$Confocal\ Parameter = 2 * ZR$$

Table 2.17 shows the confocal parameter and efficiency results for different focal length lenses assuming a starting beam diameter of 1.76mm. The values were calculated using the equations above, the measured and calculated values of the 1040nm incident pulse, and SNLO software. The actual efficiency for each lens was then measured and compared to the simulated value.

Focal Length (mm)	30	45	75
Confocal Parameter in Crystal (mm)	3.56	8.02	14.26
Simulated Efficiency (%)	36	39	32
Measured Efficiency (%)	18	13	9

Table 2.17 – SHG Performance for Various Focusing Lenses.

From Table 2.17, the 45mm focal length lens had the highest simulated efficiency, but the highest measured efficiency was obtained with a 30mm focal length lens. In the setup, a Thorlabs AC254-030-B-ML 30mm achromatic doublet was used to focus the light and a Thorlabs AC254-075-A-ML 75mm achromatic doublet was used to recollimate the green signal output. The maximum green light power was achieved through careful alignment. The degrees of freedom used to maximize the power of the second harmonic beam were the 1040nm beam polarization, the Z and X translation of the crystal, the tip/tilt of the crystal, and very fine

changes to the distance between the gratings. The green light output is characterized below in Figure 2.18 and 2.19.

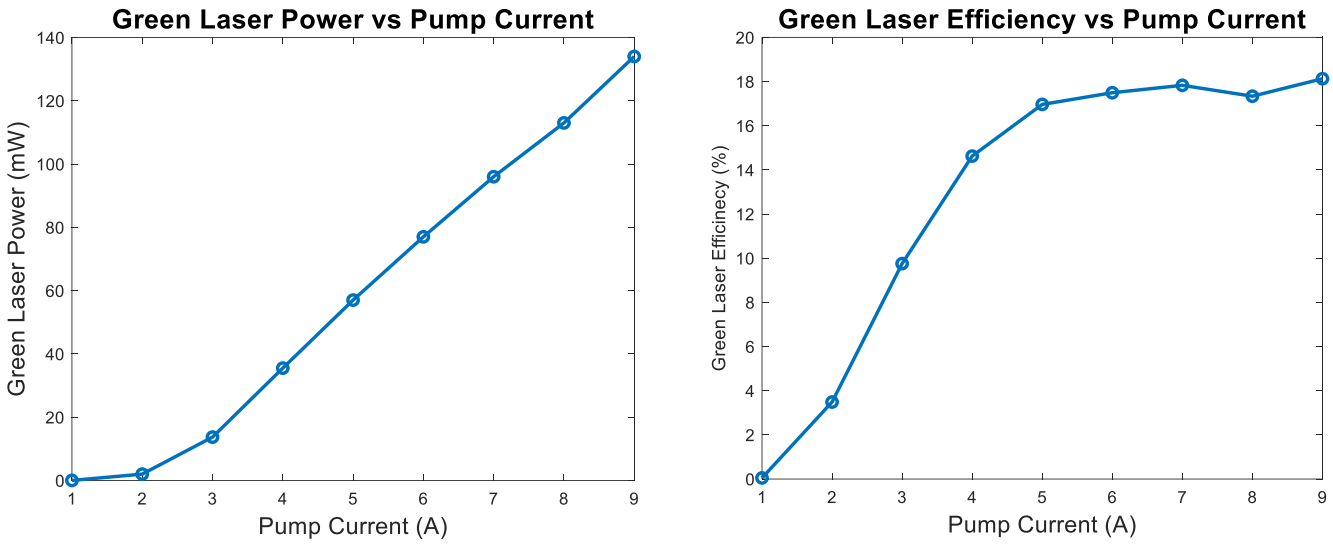

Figure 2.18 – (Right) - Green laser power and (Left) - Efficiency characterization

Figure 2.18 (Left) shows the power of the green laser as a function of the main pump current. After alignment at low power to maximize the green signal, running at the highest pump current (9A) gave a maximum power of 134mW measured with a Newport silicon detector. The efficiency (Right) shows that at maximum power there is 18% efficiency coming from the crystal. This value is lower than the simulated values for second harmonic generation from the 4mm LBO crystal. The low efficiency could be due to residual 976nm pump entering the crystal, which would slightly influence the input power values and therefore the calculated efficiency. If only the power coming from the 1040nm light is considered, the efficiency increases to 21%. The simulation also used a transform limited beam, which would cause higher values for simulated efficiency than the realistic output. There were also many sources of loss in the system leading to lower 1040nm power which would lead to lower 520nm generation. The residual pump that was not absorbed in the main amplifier gain fiber accounted for around 15% of the total measured power. Adding more gain fiber to absorb that pump would lead to a higher power 1040nm output and perhaps more power out of the crystal. At each free space component there was a small amount of loss that quickly started to add up and impact the results. The isolator

contributed around 20% loss right after the collimator due to the polarizing beam splitting cubes. The laser output was polarized, but the off the shelf combiner which combines the signal from the pre-amplifier and the main pump caused the PER to drop from around 20 to 11. A different combiner that does not depolarize the beam as much would lead to improved transmission through the isolator. Next, there was about 35% loss through the double pass grating pair. A new pair of gratings without any damage to the surface or grating structure, optimized for 1040nm light could improve the transmission. Though the 134mW of generated green light is lower than the simulated value, it is more than enough to make this microscope a versatile instrument for imaging and material science.

To finish the characterization of the green laser, the spectrum was taken using a prism oriented at Brewster's angle to transmit the maximum amount of light and spread the green light apart from residual 1040nm or 976nm components of the NIR laser. Viewing the output of the prism at Brewster's angle showed only a single beam, which is indicative of effective filtering of residual pump light. A spectrum taken with the Ocean Optics QE65000 Spectrometer confirmed that the power was coming from the 520nm beam and different spectra were captured at different pump currents as seen below in Figure 2.19.

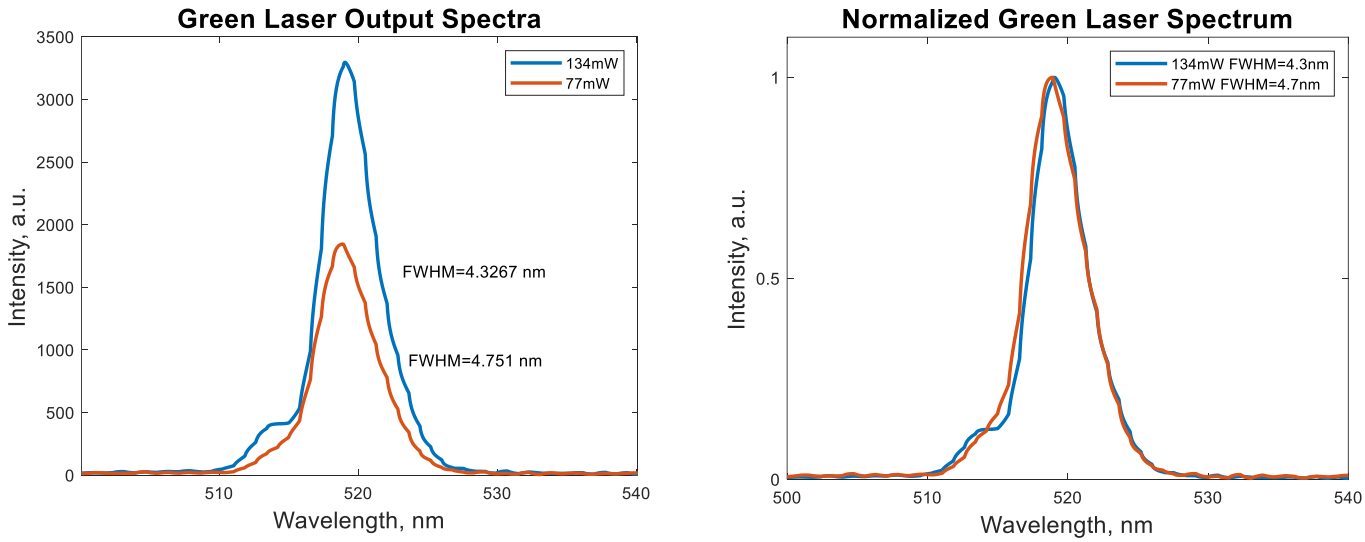

Figure 2.19 – Spectra of green laser output at different pump currents. (Left) – Unnormalized, (Right) – Normalized to show the different pulse shapes

Figure 2.19 shows the different spectra at different powers. The image on the left shows the spectrum centered at 520nm for different pump currents. The image on the right shows the two plots normalized to see the difference in intensity profiles at different power levels. At the highest pumping power (9A), the FWHM is 4.3nm which is indicative of a pulse that has a length of ~100fs. Figure 2.20, below, shows the characteristics of the generated green laser.

Average Power	Repetition Rate	Pulse Energy	Pulse Width	Peak Power
134mW	50MHz	2.6nJ	~100fs	26.8kW

Table 2.20 – Green laser specifications

The green laser specifications from Table 2.20 show promising results for multiphoton microscopy due to the high peak power and the short pulse duration.

Acknowledgements

We would like to thank Orkhongua Batjargal for her contribution to this project. The project would not have been completed without her time spent performing SNLO simulations for different crystals, selecting the crystal, and answering any questions that came up during the process of building the laser. Additionally, we would like to thank Josh Magnus for many useful discussions about the construction of the laser and assisting with many measurements, including but not limited to the autocorrelation to measure the pulse width. Lastly, we would like to thank Lam Nguyen for his help during the design process.

3. Design of the Visible Multiphoton Microscope

The nonlinear optics and ultrafast fiber laser group at the Wyant College of Optical Sciences has built many femtosecond pulsed fiber lasers and multiphoton microscopes in house. Compared to a typical MPM with a NIR source, the visible system has the advantage of higher resolution and working with standard focusing optics to illuminate the sample, but the drawback of additional loss due to the challenge of detecting light in the UV. Figure 3.1 below shows a schematic of the visible MPM, which will be further described in the following sections.

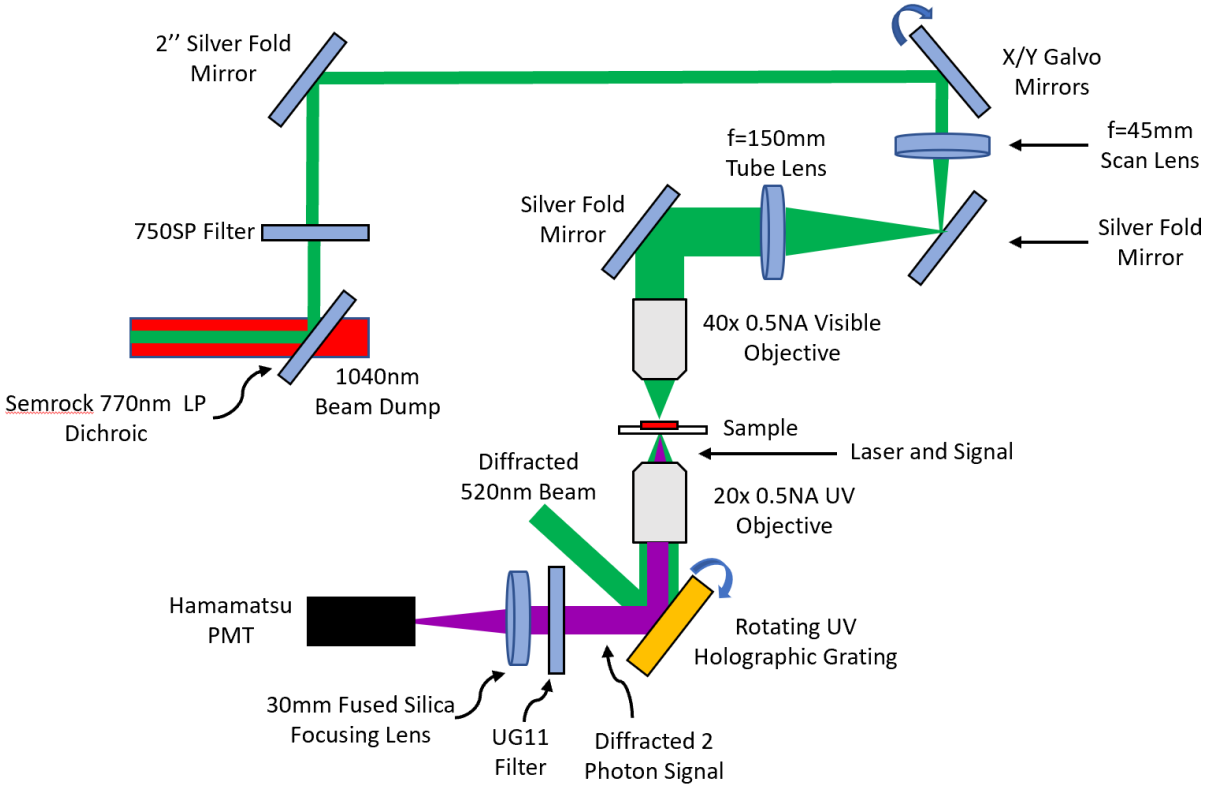

Figure 3.1 – Visible Multiphoton Microscope Schematic

Figure 3.1 shows the schematic of the visible MPM. Starting on the left, the red and green beams represent the 1040 and 520nm output from the LBO crystal as characterized in the previous section. The 1040nm beam is separated from the 520nm signal using a Semrock 770nm LP dichroic mirror which will transmit the IR light and reflect the visible. A Semrock 750SP filter is also used in the visible beam path to absorb any remaining IR light that was reflected.

The dichroic mirror acts as the first fold mirror in a two-fold mirror system that will be used to align the green beam with the microscope and send the signal to the galvo mirrors. Following the second fold mirror, the galvos will raster scan the beam in X and Y such that the focused point from the visible objective is scanned across the sample. The light reflects off the galvos and is focused by a Thorlabs AC254-045-ML-A 45mm lens that acts as the first lens in a 4x beam expander system. The scan lens is positioned such that the beam expanding system will also use the galvos as an object and image them to the back of the microscope objective to minimize aberration and maximize the field of view (FOV). Due to limited space in the microscope box, another pair of fold mirrors was used to fold the beam path. The light reflects off a silver coated 45 degree fold mirror and is collimated by a Thorlabs AC254-150-ML-A 150mm tube lens that completes the 4x beam expander. The lenses are positioned so the beam is recollimated, reflects off a fold mirror, and fills the back aperture of a high-quality Olympus 40x 0.5NA objective that will tightly focus the light on to the sample. The sample will sit on a cover glass slide and the signal will be collected in transmission by a 20x 0.5NA UV objective. The transmission detection system is unique compared to the existing NIR MPMs, as the current systems use the imaging objective to collect the nonlinear signal in an epi-detection setup. The UV objective is made of fused silica and will transmit both the 520nm laser light and the 260nm 2-photon signal. Commonly, dichroic mirrors and bandpass filters are used to separate the nonlinear signal from the laser source, but these components in the UV suffer from limited availability, higher price, and low transmission. To counter this, a Thorlabs GH25-06U UV Reflective Holographic Grating on a rotational mount was chosen to separate the signal from the source. Since different wavelengths will diffract at different angles, for a given incident angle, the signal will be clearly separated from the pump which will eliminate the need for additional UV optics in the beam path. With a properly oriented grating, the UV signal will diffract 90 degrees from the incident beam and travel to a lens tube with a UG11 filter to get rid of any additional 520nm light, a Thorlabs LA-4052-ML collection lens to focus the light on the face of the PMT, and a Hamamatsu PMT that is sensitive to UV light. A LabView code that was written by the lab group will control all of the hardware and capture an image.

3.1 Visible MPM Literature Review

There are many microscope systems published that can effectively image in the UV, each with their own distinct advantages and disadvantages. Ojaghi et al. published the design of an effective UV microscope for the assessment of Neutropenia, a blood disease [36]. Since this system relies on direct UV illumination from a plasma source, it has the drawback of requiring a UV objective for epi-detection which will have worse performance than a high-quality visible objective due to the limited glass types that transmit UV light. In addition, this microscope does not have the capability to image through depths, as the samples need to be sliced very thin to obtain an image. Lastly, the direct illumination leads to an increased risk of photobleaching. Kumamoto et al. describe a DUV Raman microscope used to image different nucleic acids and proteins at a high resolution [37]. This system uses an Argon source that is frequency doubled with a BBO crystal to directly illuminate the sample with UV light. The source wavelength is tunable with an OPO to image different Raman signals, but this comes at the cost of complexity and size. This system also uses direct UV illumination, which cannot inherently produce nondestructive 3D images. Unlike the previously described systems, UV confocal and multiphoton microscopes can image in three dimensions. It is common for these systems to use a Ti:Sapphire laser and an OPO to illuminate the sample with visible light. These described systems perform well, but are very expensive, large, and difficult to operate. Another drawback is that the imaging depth of the UV confocal systems are limited by the power out of the OPO, which is lower than the power demonstrated in Section 2 from the fiber amplifier and LBO crystal [33,34,35]. This is not as much of a problem in UV multiphoton microscopy, where signal is only generated in the focal volume of the objective lens. Unlike other types of UV microscopes, UV MPMs make use of transmission detection systems which utilize a high-quality visible objective to focus the sample. A common UV MPM transmission detection system involves placing a large area PMT physically as close to the sample as possible, with only thick filters to absorb the residual visible light [38,39,40]. This setup with no collection optics causes transmission loss as the PMT is placed further from the objective. Additionally, the lack of space between the sample and the detector limits the detected signal to one-channel, typically 2PEF [38,39,40]. The microscope described in this thesis has advantages to current systems due to the high power, robust source, and the flexible transmission detection system.

3.2 Optical System Design

This section will review the detail and characterization of the design of the visible MPM. The main two components of the MPM are the illumination and detection branch. The illumination branch was analyzed for optical performance in Zemax which includes an aberration and tolerancing analysis. On the detection side, four different detection schemes were analyzed to try and find the best solution to detect the UV signal.

3.2.1 Illumination Branch

The optical design of the illumination branch of the visible MPM is no different from existing NIR designs. A collimated beam is sent to a two-element lens system made up of two achromatic doublets that serves two purposes. The first is to expand the beam to fill the back aperture of a microscope objective. This ensures the full use of the objective NA for the highest resolution imaging. The second purpose is to image the galvo scan mirrors to the back of the objective such that all scan angles are supported without vignetting. This will lead to the largest attainable FOV for the microscope given the optics in the illumination path. The collimated, expanded beam is then focused on the sample by the microscope objective. The optical system prescription detailing the lenses and the distance to the next optical element is below in Figure 3.2.

Element Description	Off-the-Shelf Part Number	Focal Length	Distance to Next Element
Galvo Scan Mirrors	Thorlabs GVS002	Infinity	30.206mm
Scan Lens	Thorlabs AC254-040-A-ML	40mm	77.0mm
Fold Mirror	Thorlabs CCM1-P01	Infinity	102.38mm
Tube Lens	Thorlabs AC254-150-A-ML	150mm	58mm

Fold Mirror	Thorlabs CCM1-P01	Infinity	180mm

Table 3.2 – Optical System Prescription

Figure 3.2 shows the system prescription detailing each optical element. The last fold mirror acts to send collimated light to the visible objective. A tolerancing analysis, which will be discussed later in this section, will give important information about the sensitivity of the position and alignment of the optics. The element spacings from the table above were determined in Zemax and a model of the folded 4x beam expander system is seen below

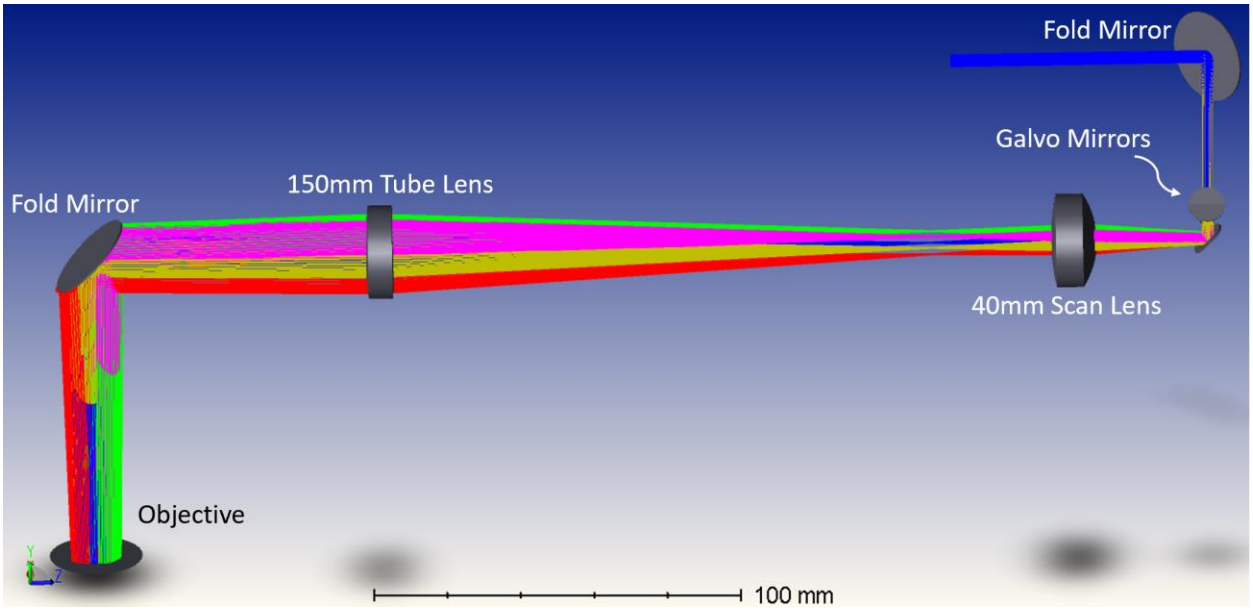

.

Figure 3.3 – 3D Shaded View of the Beam Expanding System in Zemax

Figure 3.3 shows the 3D shaded view of the 4x beam expander in Zemax. To try and realistically model the system, multiple configurations were setup with different galvo mirror scan angles. The different colored beams that are seen in the figure (red, green, gold, pink, blue) represent different galvo scan angles over a 5 degree FFOV. The galvo mirrors were defined as the system

stop due to their control over the off-axis ray bundle, and therefore accurate modeling of the scanning setup was necessary to properly analyze the aberration and potential vignetting. Using an afocal image space to analyze the collimated output towards the objective lens, spot diagrams and OPD plots were generated to analyze the system performance.

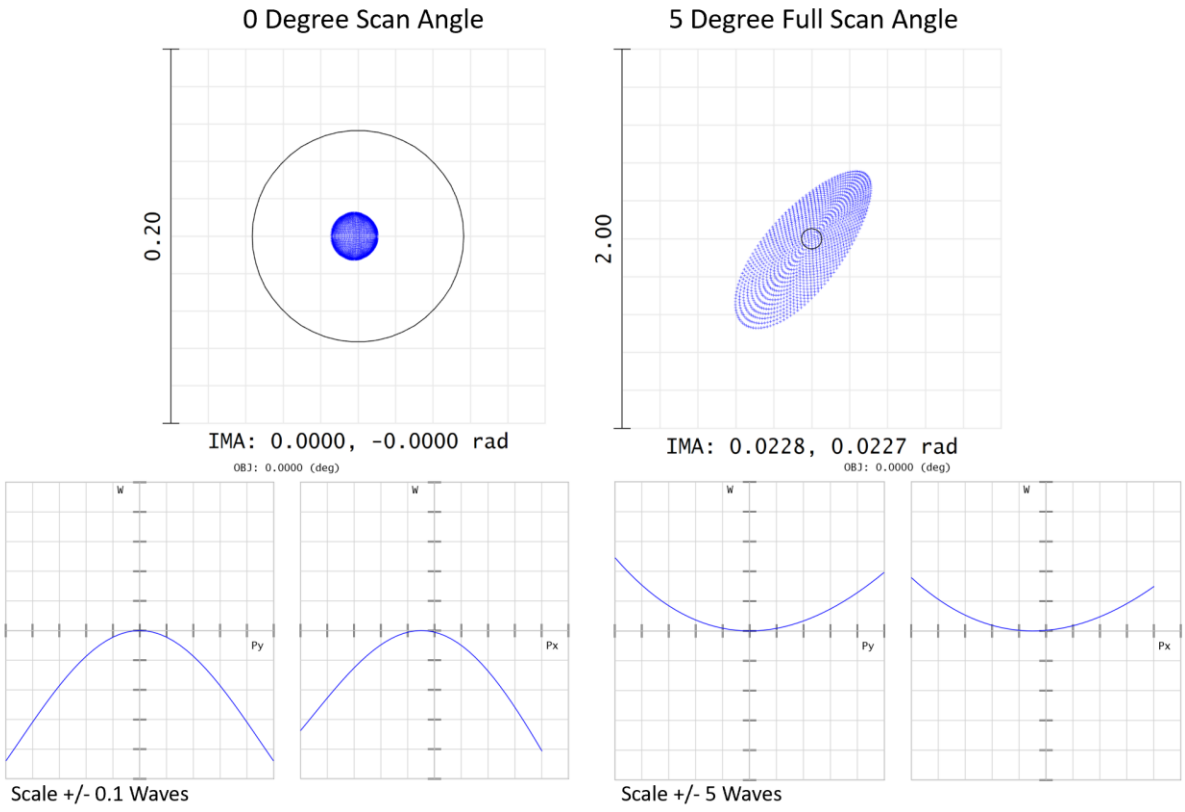

Figure 3.4 – System performance in Zemax. (Left Column) – On-axis performance from a 0 degree galvo scan angle showing the spot diagram (Top) and the OPD plot (Bottom). (Right Column) – System performance for a 5 degree full galvo scan angle. (Top) – Spot diagram. (Bottom) – OPD plot.

Figure 3.4 shows the system performance. From the figures on the left, the on-axis performance is diffraction limited, but as the galvo scan angle increases to the 5 degree FFOV, aberrations become much more prominent. The main aberrations from the spot and OPD plots at the 5-degree FFOV are spherical aberration, astigmatism, and field curvature. These aberrations are prominent due to the use of off the shelf components. Off the shelf components were selected due to their low price and easy availability, but at the cost of fewer degrees of freedom for

correcting aberration in a system. For example, spherical aberration can be corrected by lens bending and lens splitting, which is not possible with a single component with fixed radii. The best that one can do to correct for spherical aberration in the given setup is change the orientation of the lens such that the rays bend an equal amount at each surface. To minimize spherical aberration the scan lens has its more curved side oriented towards the collimated light and the tube lens has its planar side facing the diverging beam. To further correct for spherical aberration, custom lens elements can be designed for a higher price, or multiple off the shelf lenses can be used to make up a single element. For example, two 80mm focal length lenses could be placed in succession with the proper orientation to model a 40mm scan lens with less spherical aberration. Another prominent aberration in the system is field curvature. Field curvature occurs when the rays do not focus to an ideal image plane, but rather focus along a curve, the Petzval surface. Field curvature has a large impact on the maximum scan angles that the relay system can accommodate. The total amount of field curvature in a system is equivalent to the sum of the power over the index of refraction for each surface, so using a mixture of positive and negative elements will greatly reduce the Petzval sum. If custom elements are not an option, Thorlabs has scan and tube lenses designed for wide scan angles in laser scanning microscopy applications. Though more expensive, the specially designed scan lens is designed to have a flat image plane and will provide a uniform spot on the focal plane for all scan angles. The telecentric scan lens paired with an infinity corrected tube lens would create a high performing off the shelf system that could accommodate large scan angles.

Figure 3.4 analyzes the performance of the ideal optical system, but realistically lenses will be slightly displaced, decentered, and tilted which will further impact the imaging performance. Though the elements will be mounted in a cage system, a tolerance analysis is still useful to identify the components that require the most attention while aligning, while also analyzing the more realistic performance of the microscope. The parameters that were used in the Zemax tolerancing analysis are listed below in Table 3.5 and the results are listed in Figure 3.6.

Tolerancing Variable	Element	Minimum Value	Maximum Value
Y-Tilt	Tube Lens	-1 Degree	1 Degree
X-Tilt	Tube Lens	-1 Degree	1 Degree
Y-Decenter	Tube Lens	-2mm	2mm
X-Decenter	Tube Lens	-2mm	2mm
Y-Tilt	Scan Lens	-1 Degree	1 Degree
X-Tilt	Scan Lens	-1 Degree	1 Degree
Y-Decenter	Scan Lens	-2mm	2mm
X-Decenter	Scan Lens	-2mm	2mm
Scan to Tube Lens Separation	Scan Lens	-2mm	2mm
Galvo to Scan Lens Separation	Galvo Mirrors	-2mm	2mm

Table 3.5 – Tolerancing analysis parameters in Zemax.

Table 3.5 shows the different variables in the tolerancing analysis. For the purpose of analysis, a paraxial lens was added so the RMS wavefront could be analyzed for all configurations. The paraxial lens adds no additional aberration and only works to focus the collimated beams to a point. 10,000 Monte Carlo trials were run with a uniform distribution. The Monte Carlo analysis output in Figure 3.6 shows that this system will still perform well with minor misalignments. The nominal value +/- 2 standard deviations predicts a working RMS wavefront error of 0.317 waves, which is a good indicator that the system will perform well as built.

```
Nominal         0.26080904
Best            0.22128267   Trial   2460
Worst           0.42289114   Trial   8459
Mean            0.28864398
Std Dev         0.02843036

    98% >       0.34735186
    90% >       0.32783018
    80% >       0.31403064
    50% >       0.28718735
    20% >       0.26379199
    10% >       0.25126996
     2% >       0.23493526
```

Figure 3.6 – Output of Monte Carlo trials for Zemax tolerancing analysis

In Figure 3.6 above, the exact tolerancing values are shown which gives valuable insight in to how the system will perform with minor misalignments that could occur during construction.

3.2.2 Detection Branch

The design of the detection system for the visible MPM is not trivial due to the limited materials that will transmit UV light. The first detection scheme that was considered was an epi-detection system that uses a UV objective to focus the source and then also collect the signal. The signal and the source would then be separated using dichroic mirrors and filters as seen below in Figure 3.7.

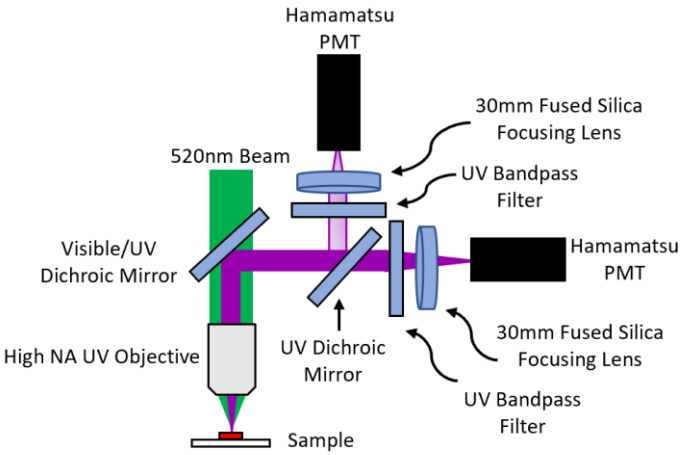

Figure 3.7 – UV epi-detection schematic

Figure 3.7 shows the schematic for a UV epi-detection system. The main component of this detection system is the UV objective that focuses the visible light on to the sample, collects the UV light, and then sends the signal to two PMTs using various dichroic mirrors and bandpass filters. An advantage to this system is that the NIR MPMs in lab use this detection setup, so it is proven to work well and requires minimal alignment. The two PMT setup allows for two different signals to be detected simultaneously (ex: SHG, 2PEF). This all comes at the cost of lower image quality with only a UV objective. Since there are only a limited number of materials that transmit DUV light, a UV objective will produce lower quality images and ultimately lead to worse imaging performance. This system also relies on the use of dichroic mirrors and bandpass filters to separate the UV source from the visible source which can be very expensive and have low transmission at lower wavelengths.

The next detection system analyzed is a transmission detection setup that commonly showed up in the literature [38,39,40]. This detection scheme, shown in Figure 3.8 uses a visible objective for higher image quality with a PMT as close to the sample as physically possible to maximize the collection efficiency.

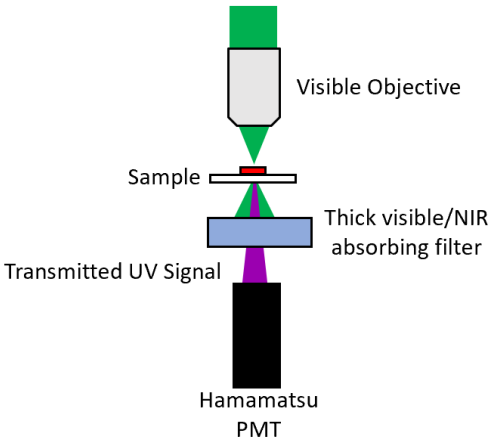

Figure 3.8 – UV transmission detection system with only a PMT.

As seen in Figure 3.8, a thick absorbing filter is placed between the sample and the PMT to absorb any residual visible or NIR light. This setup uses the fewest components and is easy to align, but it is dependent on the PMT being as close to the sample as physically possible with only a thick absorbing filter in between. This constraint limits the detection scheme to only one signal at a time and potentially very low efficiency depending on the detector position. In this scheme, the amount of light collected is a function of the solid angle subtended by the detector at focus [39]. The equation for the NA of the 8mm PMT is seen below.

$$NA = \sin(\arctan\left(\frac{PMT\ Radius}{Distance\ from\ Focus}\right))$$

Relating the solid angle of the PMT to the NA,

$$\Omega = \pi * {NA_{PMT}}^2 * Tfilter$$

Assuming a perfectly transmitting filter, Solid angle can be rewritten in known terms as

$$\Omega = \pi * \sin^2\left(\arctan\left(\frac{PMT\ Radius}{Distance\ from\ Focus}\right)\right) * Tfilter$$

Using the above equations for the NA and solid angle of the PMT and an objective with a known NA, the collection efficiency can be plotted as a function of distance from the detector given the dimensions of a PMT that is on hand in lab.

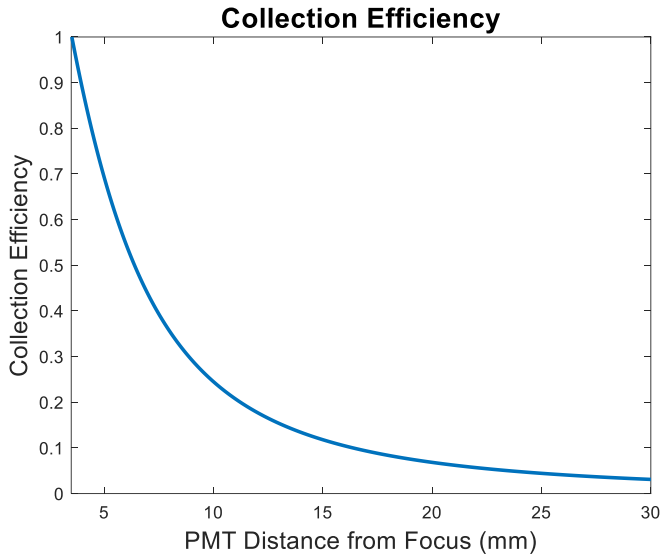

Figure 3.9 – Collection efficiency of the straight transmission detection system

Figure 3.9 shows how rapidly the collection efficiency decreases in this setup. After only 10mm, the efficiency is down to 20%, and there needs to be space for at least a few mm thick absorbing filter to remove the other visible light transmitting through the sample. The efficiency values can be increased with a larger area PMT, however the lack of ability to detect more than one signal at a time is a major drawback to this detection scheme.

The third detection system that was considered was a transmission detection setup with a UV objective and dichroic mirrors/bandpass filters to separate the signal from the source.

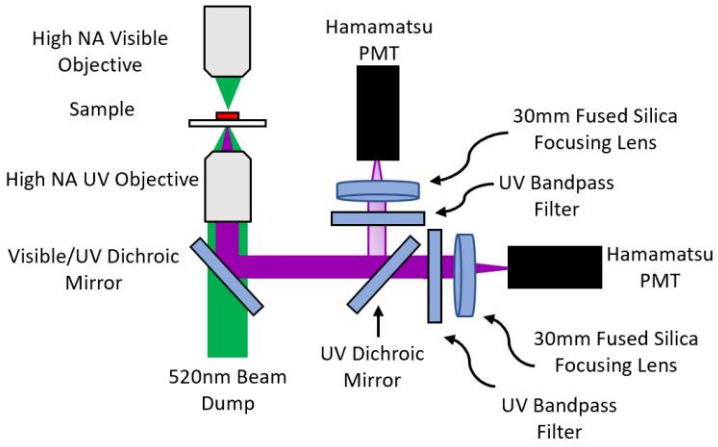

Figure 3.10 – Transmission detection system with dichroic mirrors

Figure 3.10 shows the schematic of the transmission detection system with various dichroic mirrors and bandpass filters to separate the 520nm source from the UV multiphoton signal. This design uses a high NA visible objective to focus the visible source on to a sample. The use of the visible objective eliminates the possibility of an epi-detection setup but allows for the highest image quality which is paramount in microscopy. The transmitted visible light and the generated UV signal in the forward direction are collected by a UV objective which will be mounted on an XYZ translation stage to maximize signal collection. The UV objective will 53ecollimated the light and send the two beams to a UV/Visible dichroic mirror. The dichroic mirror will act to transmit the visible laser light to a beam dump and reflect the UV signal to be detected. The UV signal will then be separated into the desired channels (SHG, 2PEF) by UV dichroic mirrors and filters and then collected by fused silica focusing lenses to be sent to the PMTs. This setup has many advantages, a high quality visible objective gives the best image quality and the detection scheme is easy to align in a cage system. The drawbacks to this setup are the cost and availability of each of the dichroic filters and mirrors in the UV.

A detection scheme that could separate the visible and UV light without the use of dichroic mirrors and filters would greatly reduce the overall cost. An optical element such as a prism or diffraction grating can physically separate beams of different wavelengths and are commonly used in spectrometry applications. Due to the limited space under the microscope

stage for detection, a reflective diffraction grating was chosen as the best option. The schematic for the final detection option is seen below in Figure 3.11.

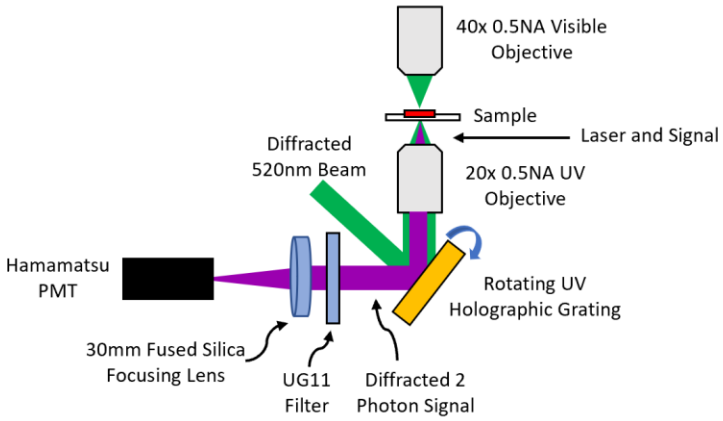

Figure 3.11 – Detection scheme with diffraction grating

Figure 3.11 shows the detection scheme without the use of dichroic mirrors. Like the previously described setup, this uses a visible objective for high image quality and a UV objective to collect the transmitted source and signal. After the UV objective, a Thorlabs 600lp/mm UV Holographic grating is mounted on a manual rotation mount and oriented at an angle such that the UV signal reflects and diffracts 90 degrees from the incident beam and the 520nm source reflects and diffracts at a different angle such that it misses the detection components entirely. The holographic grating was chosen because it has very little stray light and cross talk between diffracted orders compared to a ruled grating. This stray light control comes at the cost of high efficiency, but the efficiency of the grating at 260nm is still around 60%. This setup is advantageous because it is cheaper, easy to align, and requires fewer components since the diffraction grating replaces the dichroic mirrors and bandpass filters. For additional filtering, bandpass filters can be used before the PMT in the UV light path. Future work can be done to make this a detection scheme that detects multiple signals at once with careful PMT positioning based on the wavelength of the detected signal, or potentially with dichroic mirrors, bandpass filters, and collection lenses. Future work can also be done to automate the detection process.

Using the grating equation,

$$\alpha[\sin(\theta_m) + \sin(\theta_i)] = m\lambda$$

α represents the grating spacing, θ_m represents the diffracted angle, θ_i represents the incident angle, m represents the diffraction order, and λ is the wavelength. The diffracted angle vs incident angle can be plotted for m=1 to figure out the proper grating orientation. The resulting plot is shown below in Figure 3.12.

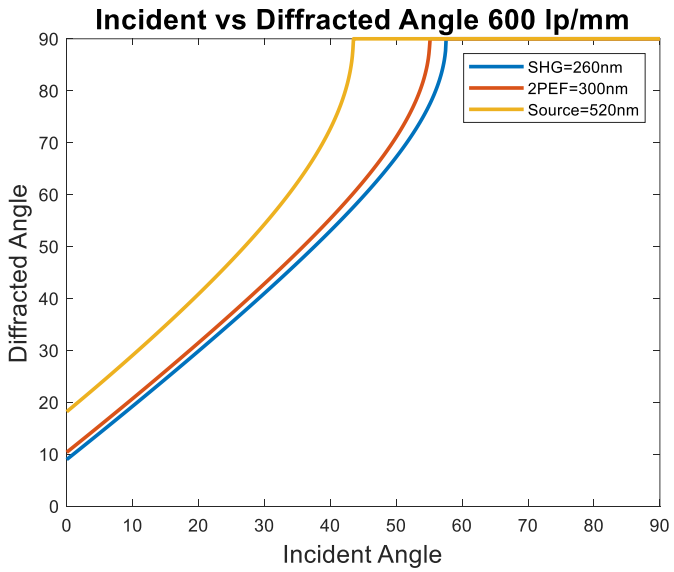

Figure 3.12 – Incident vs diffracted angle for the 600lp/mm UV holographic grating

Figure 3.12 shows the different diffraction angles for important wavelengths in the system. 260nm is SHG signal, wavelengths longer than 260nm is 2PEF, and 520nm is the source light. From the plot and using Matlab, values can be extracted to determine the grating orientation that is suitable for the visible MPM. The data is seen below in Table 3.13.

Wavelength (nm)	Incident Angle (Degrees)	Diffracted Angle (Degrees)	Sum of Incident and Diffracted Angles (Degrees)
260	38.64	51.31	89.95
260	37.65	50.08	87.73
300	38.64	53.56	92.2
300	37.65	52.27	89.92
520	38.64	69.48	108.12
520	37.65	67.36	105.01

Table 3.13 – Diffraction grating position for SHG/2PEF signal detection

Table 3.13 shows the angle of grating orientation that should be used to send SHG and 2PEF at a 90 degree angle from the starting beam, which will send the desired signal towards the PMT. When detecting SHG, the grating will be set at 38.64 degrees to send SHG 90 degrees total to the PMT. At this grating orientation, the 2PEF signal at around 300nm will deviate 92.2 degrees, which is close to the SHG beam so an additional bandpass filter may be necessary, or even a dichroic mirror and a collection lens to detect the 2 signals simultaneously. Similarly, to detect only the 2PEF signal, the grating should be oriented at 37.65 degrees. When the grating is oriented for SHG and or 2PEF, the source beam will have deviated a total angle of 108.12 and or 105.01 degrees from the initial source direction. This is a large enough angular difference for the beam to miss the PMT and collection optics entirely, so no additional 520nm filtering is necessary. If necessary, a pinhole or knife edge can also be used to further block unwanted diffracted orders.

3.3 Microscope Construction

Now that the optical design of the illumination and detection system have been laid out, it is time to construct the microscope. The microscope will be housed in an 18in x 18in x 18in black box so the PMTs can operate in a dark environment. There will be a hole cut in the side so the beam can enter from the free space optics. The majority of this construction uses a Thorlabs cage system for easy alignment of the optics. The galvo mirrors, scan lens, tube lens, and fold mirrors were all mounted in their proper positions on a cage system before being mounted to two cage clamps on elevated posts. It is important that the fold mirrors be mounted in cage cubes so the entire illumination system could be one piece and have cage rods for the clamps to attach to.

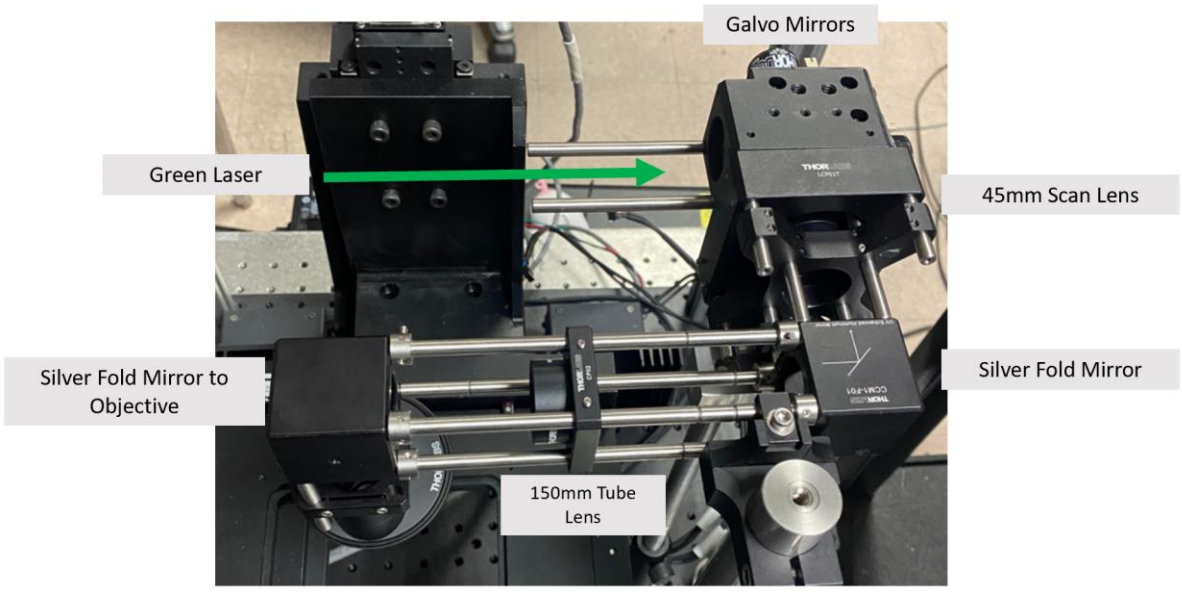

Figure 3.14 – Bird's eye view of the mounted illumination optics

Figure 3.14 shows a top view of the illumination optics described above. The cage system allows for easy mounting and minimal alignment. Various cage rod sizes were put together to place the fold mirror to the objective at the center of the stage. A side view of the same optics, shown below in Figure 3.15, is useful to see the mounting of the visible and UV objectives as well as the posts and cage rods used to secure the optics to the breadboard.

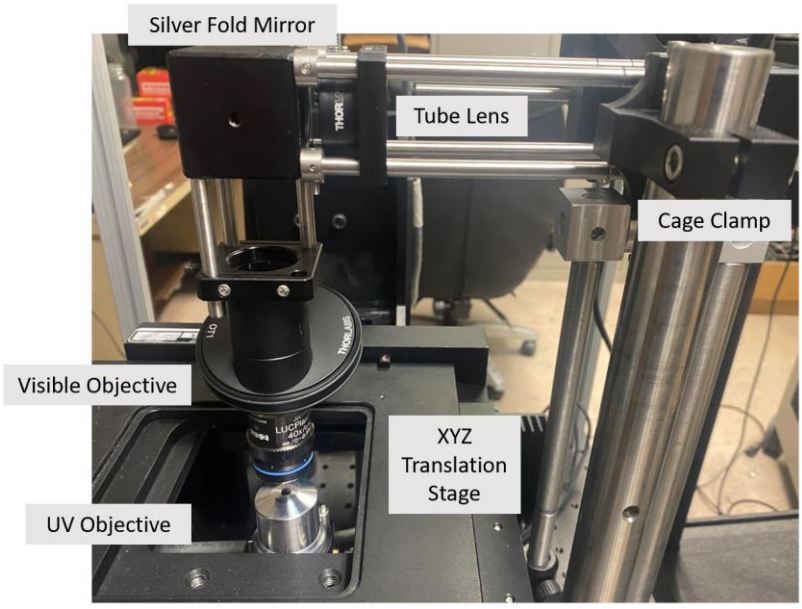

Figure 3.15 – Side view of the illumination optics

From the side view in Figure 3.15, we can see the fold mirror to the objective centered on the XYZ translation stage. The importance of a mounted cage cube is shown as the objective is centered on the stage as well with minimal alignment. The objective is connected to a turret, which will allow for quick switching between objectives for imaging with different magnifications and numerical apertures when necessary. At the bottom of the image, there is also the first glimpse to the start of the detection branch with the UV objective. The UV objective is also mounted on an XYZ translation stage to maximize transmitted signal.

The detection system to this visible MPM is unique and careful thought was put into how it would be implemented in the microscope where there is limited space beneath the stage. The space underneath the stage was measured and each component was constructed outside of the microscope first to ensure a proper fit. The first task was mounting the UV objective. Having the proper degrees of freedom for the UV objective is very important to the overall transmission of the UV signal. The most important degrees of freedom are XYZ translation, as the cage system will secure the objective to minimize tip/tilt misalignments. Since the pupil of the UV collection objective is small, any small displacement in X, Y, or Z from the optimal position will result in loss. The design of the UV objective mount is shown below in Figure 3.16.

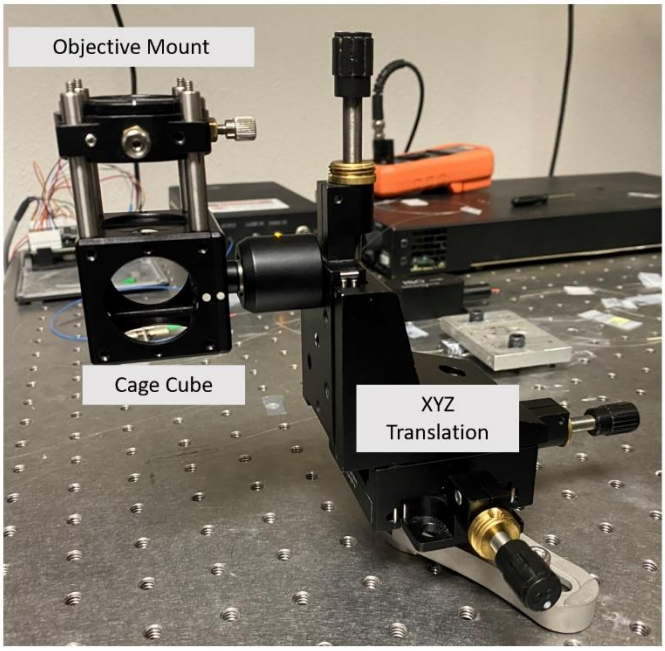

Figure 3.16 – UV Objective Mount

The mount above uses Newport translation stages to ensure proper ability to translate in three dimensions. The translation stages are mounted on a one-inch post and secured to the optical table with a clamping fork. The post is necessary to elevate the mount so that there is room for the holographic grating beneath it. A post is mounted to the translation stages and attached is a cage cube. The cage cube is very important and serves two purposes. The first purpose is to allow for cage rods for rough Z translation of the UV objective. Once the UV objective is placed in around the correct position, the fine translation of the stages can be used. The second purpose of the cage cube is to make sure there is a clear path for the collected signal to travel. This ensures that no other mounts will get in the way of the beam path and allows the translation stages to be placed off to the side so there is more room for other components in the beam path.

The next component to mount is the rotating diffraction grating. The key to this part is a rotation mount that attaches to a post oriented orthogonal to the optical table. This allows for the grating to be rotated in the desired direction and for fine control over the grating orientation. The mount can be seen below in Figure 3.17.

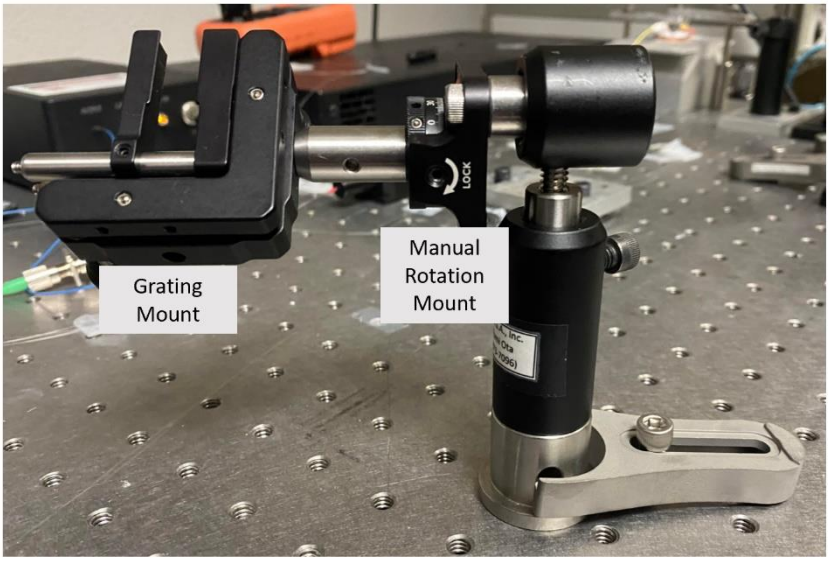

Figure 3.17 – The UV holographic diffraction grating mount

Figure 3.17 shows how the UV diffraction grating will be mounted. The base of the post attached to optical table will be secured with a clamping fork. The short post is necessary for the mount to fit under the UV objective mount. A manual rotation mount is secured with a screw to an optical post and oriented by hand such that the mount is parallel to the optical table at zero degrees. This setup allows for very fine control and easy adjustment of the grating angle which is critical for this setup. From there, the UV holographic grating is mounted in a Thorlabs grating mount.

The last part of the detection system that was assembled outside of the microscope housing was the PMT mount. The PMT mount and the optics leading up to the PMT have the purpose of relaying the optical signal to the face of the PMT and to filter out unwanted pump light. The entire PMT scheme is shown below in Figure 3.18.

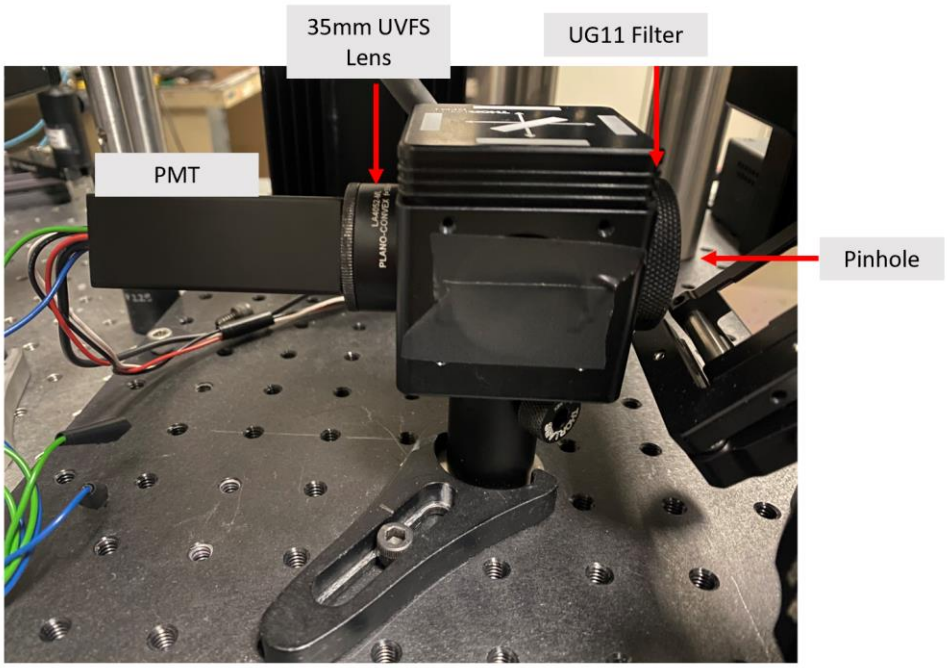

Figure 3.18 – The PMT Mount to Filter out the Visible Laser from the UV Signal

The light diffracts from the grating and enters the detection setup from the right. Due to the limited space for the mount, there is a possibility that diffracted visible light could be collected by the lens on the other side of the cube. To prevent this, a pinhole was placed on the front aperture of a Thorlabs DFM1BS cage cube to block any additional visible light. Directly after the pinhole is a UG11 filter that is used to transmit UV and block any extra visible light. The sides of the cube are blocked with black electrical tape for additional stray light control. On the other end of the cage cube is a Thorlabs LA4052-ML UV Fused Silica collection lens that will collect the UV light and focus it on to the PMT. The PMT is then mounted to a custom machined lens cap and mounted to the collection lens.

Each component of the detection system was constructed outside of the microscope and then placed in the system. The complete scheme is shown below in Figure 3.19.

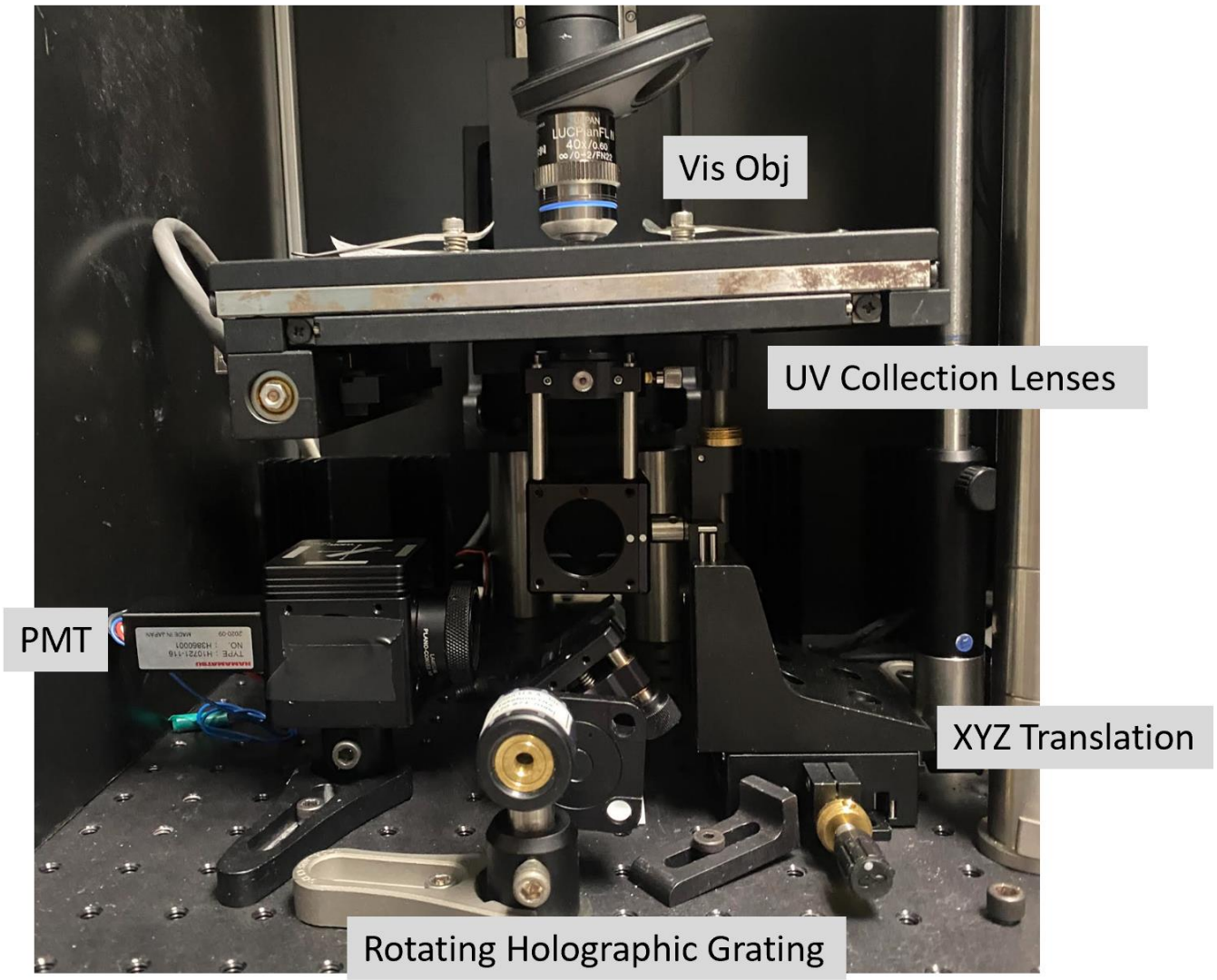

Figure 3.19 – Complete Transmission detection system

Figure 3.19 shows the complete transmission detection system. While it is a tight fit, there is plenty of space for each component due to the four-inch tall posts that the stage is mounted on. There is clear access to each of the adjustment knobs to translate the UV objective as seen on the right side of the image. The rotational grating mount fits nicely directly under the objective with a clear optical path. The PMT mount is directly to the left of the UV grating with enough space

that the grating can fully rotate and the protruding PMT on the far left still fits inside of the box. Figures 3.20 and 3.21 below are additional images showing the complete system.

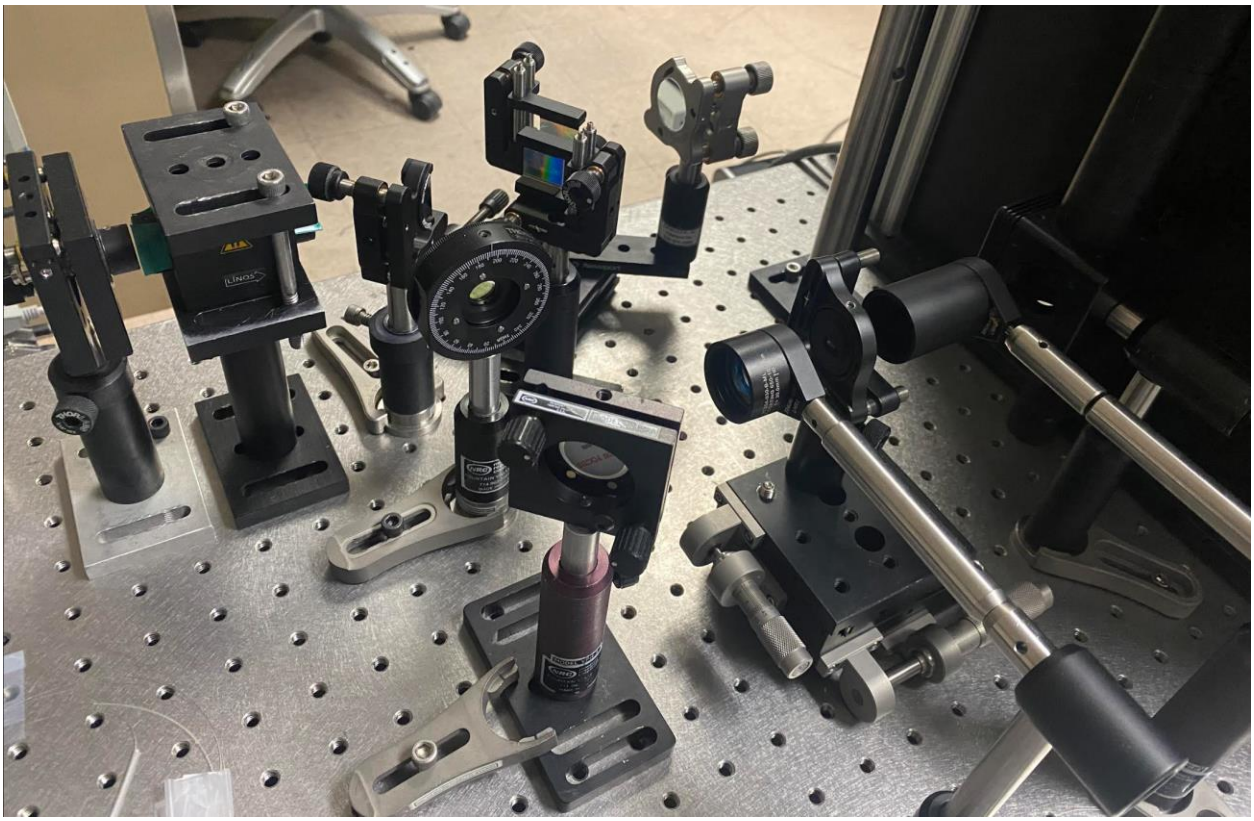

Figure 3.20 – The optical table setup of all of the free space components. The grating pair compressor can be seen at the top of the image followed by the elements that focus the light through the crystal to generate green light at then bottom.

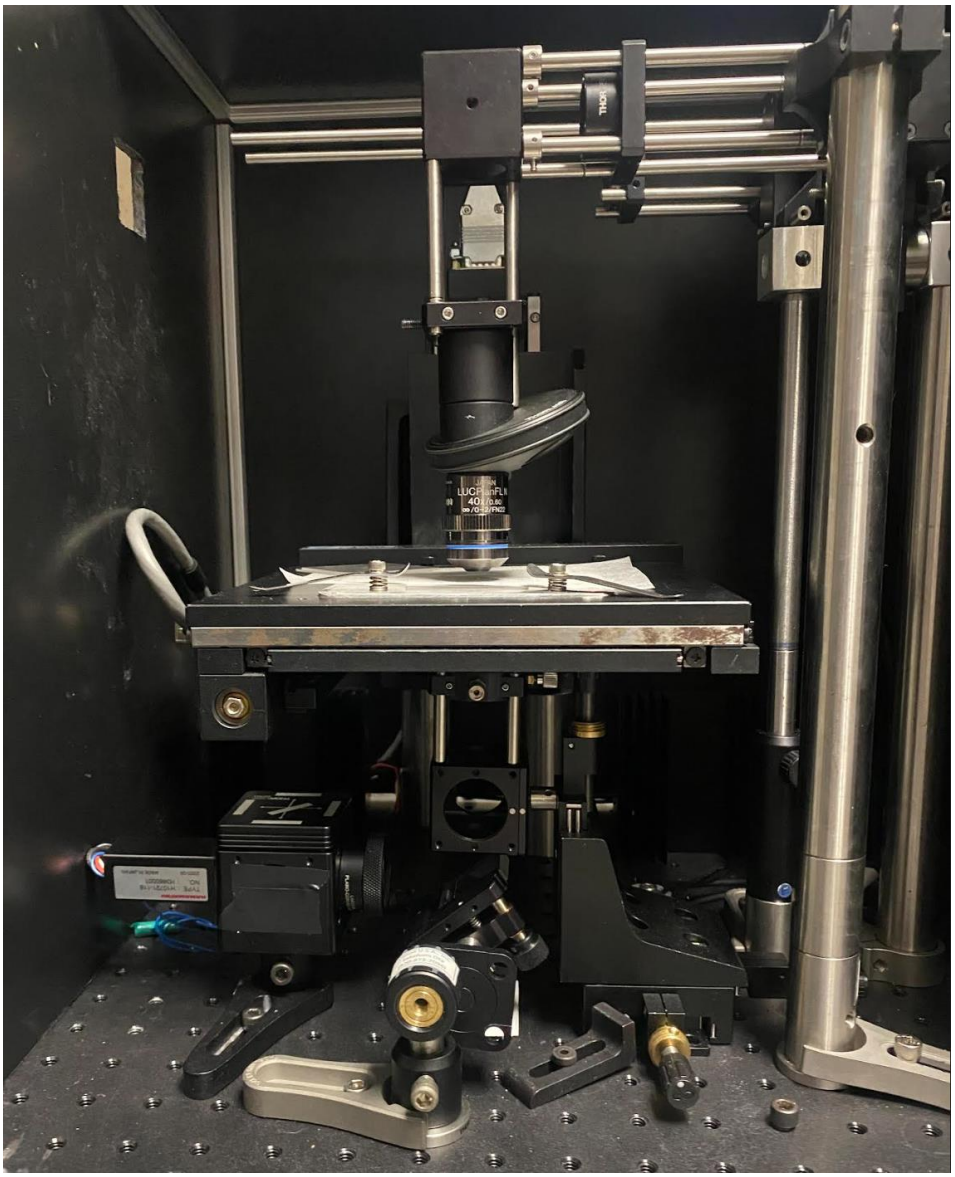

Figure 3.21 – The visible MPM. The illumination branch is at the top of the microscope with a folded beam path. The visible focusing objective and the UV collection lenses surround the translation stage and the detection optics all are mounted below the elevated translation stage.

4. Imaging Results

Now that the microscope has been built, the last steps are to obtain an image and characterize the performance. Due to the UV wavelength that is being detected, new alignment and characterization techniques must be developed. For example, to test the alignment of a NIR MPM, a slice of gallium arsenide (GaAs) may be imaged for very bright and uniform signal and the resolution can be characterized using a nonlinear knife edge test. When using a visible source, GaAs cannot be detected in transmission. For initial imaging results, an unstained sample of mouse brain tissue was mounted on a 1mm UV fused silica slide that transmits wavelengths down to 190nm. The grating in the detection system was set to a 39.5 degree angle, which was calculated to diffract the 2PEF signal 90 degrees from the initial beam path towards the PMT. Figure 4.1 shows the spectral detection system at work and the different diffracted orders at the exact grating position when an image was taken.

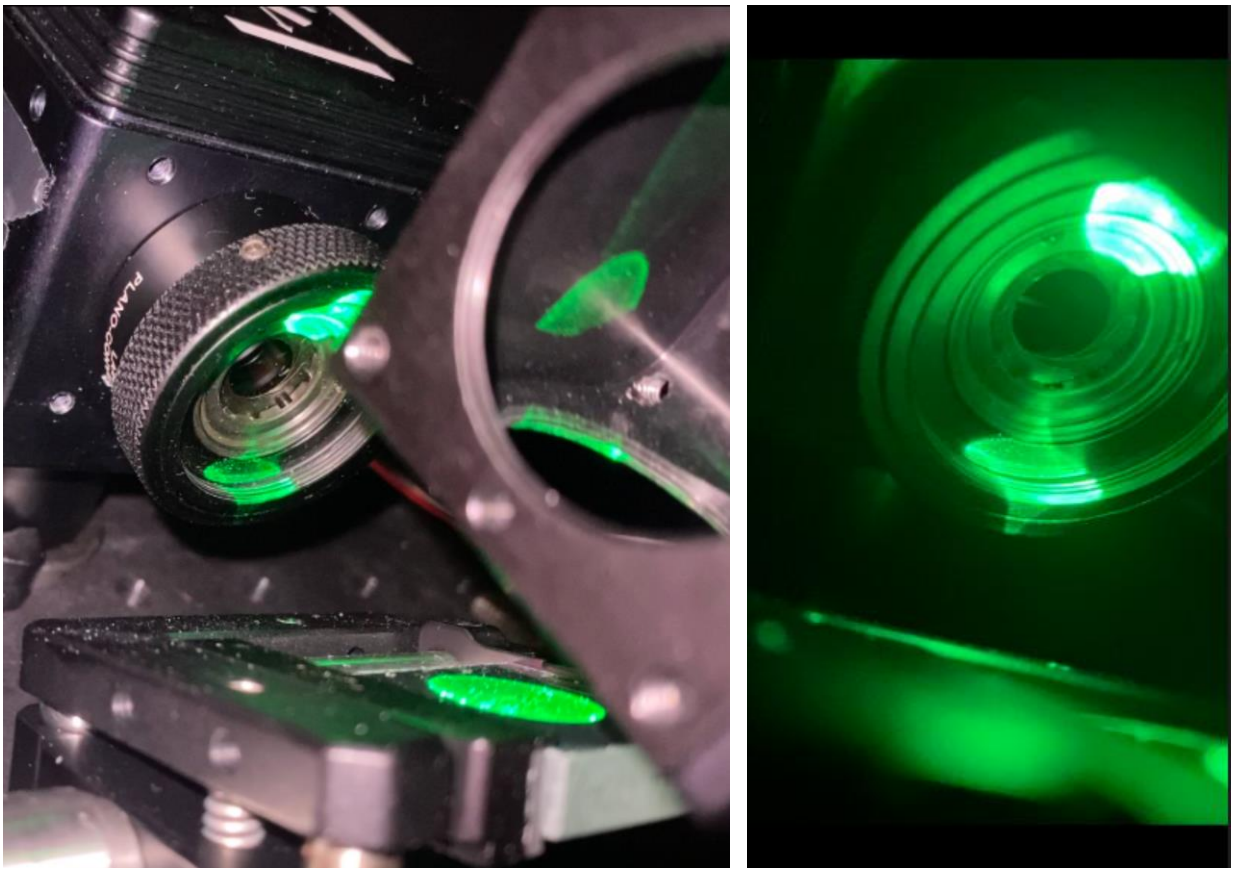

Figure 4.1 – The spectral detection setup at a grating angle to image 2PEF

Figure 4.1 above shows that when capturing an image, the m=0 diffracted order, seen by the bright green spot above the PMT, does not enter the collection lens with a partially closed aperture. The m=1 diffracted order, the dimmer green beam below the PMT is also blocked, showing that the only light directly entering the collection lens is the m=1 diffracted order from the UV signal. The following images were taken with the diffraction grating at the angle shown above.

The initial visible MPM images can be seen below in Figure 4.2.

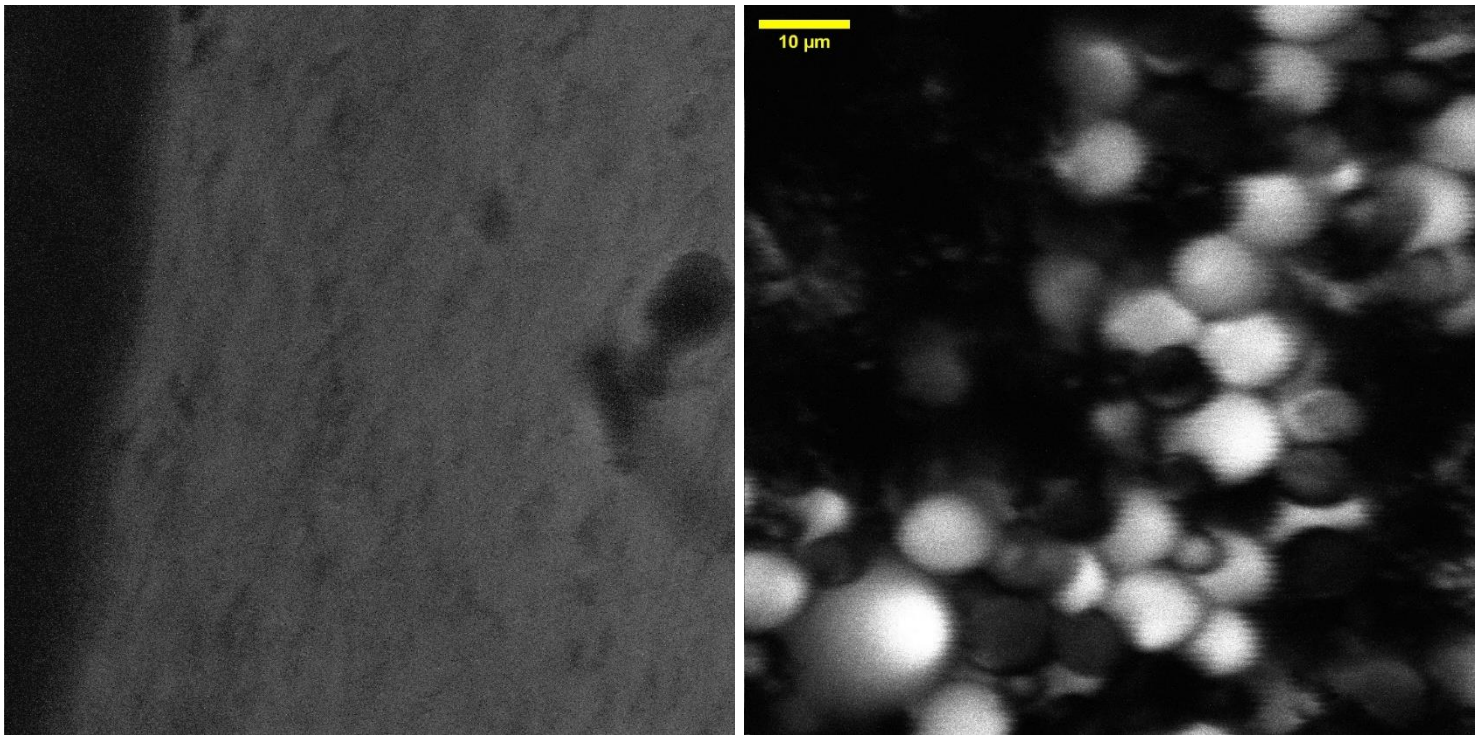

Figure 4.2 – First images with the visible MPM. (Left) – Unstained mouse brain tissue mounted on a UVFS slide. (Right) – Plastic microspheres containing polyethylene, polystyrene, and PMMA.

Both images shown in Figure 4.2 were taken with a 40x 0.75NA objective, 40mW power entering the microscope, and a UG11 filter in front of the PMT to transmit 270-375nm light. The image of the mouse brain sample on the right of Figure 4.2 shows fluorescence from the tissue. The plastic microsphere slide contains polyethylene (1-4um diameter), polystyrene (9.5-11.5um diameter), and PMMA (3-10um diameter) show strong 2PEF as well.

It is important to be able to verify that the signal from the images is in fact multiphoton signal. To do this, an OceanOptics spectrometer sensitive to 300nm was swapped with the PMT and a spectrum was taken as seen in Figure 4.3 below.

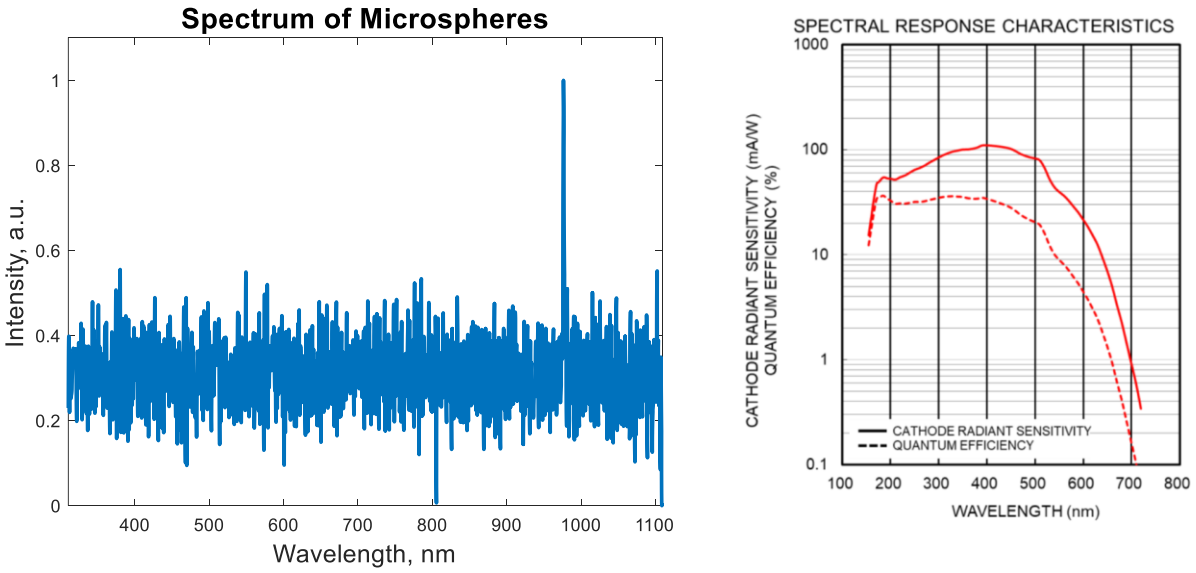

Figure 4.3 – Spectrum of Plastic Microspheres. (Left) – Spectrum of the image of the plastic microspheres. (Right) – Spectral response of PMT.

The spectrum in Figure 4.3 shows a small peak at 976nm. This is from pump light from the laser leaking through the system. This can easily be eliminated with the use of a 750SP or a 517/20 bandpass filter in the beam path. This signal does not flood the image because the PMT does not respond to that wavelength. The PMT used is custom designed for UV applications and can only detect light from 170nm-700nm. There is no peak at 520nm which would be visible if this were a single photon image of the fundamental beam. There is also no peak past 300nm, which shows the fluorescing signal from the spheres is also not over 300nm. The 2PEF signal could still be there below 300nm, as we expect to see 2PEF anywhere from 260nm and above. Further work to remove the window of the spectrometer to detect shorter wavelengths will be done to accurately characterize the UV signal. Additionally, the current setup makes it difficult to obtain a spectrum, so the use of a flip mirror in the dichroic cube for detection would make the process quicker, easier, and more accurate.

The next step is to improve the image quality of the visible MPM as the images in Figure 4.2 are not as high resolution as theoretically possible. The first step is to come up with a better alignment technique for the microscope. The current method is to use the tip and tilt on the 770nm dichroic mirror and the 2 inch silver mirror from the free space components to align the beam along long cage rails extending from the dichroic mirror. An improved system would be to additionally analyze the reflection of a flat optic on the translation stage to verify that the beam travels along the same path and the microscope is properly aligned. Another improvement to be made is to eliminate the jitter caused by the delay in the galvo scanning mirrors. This effect can be seen in the microbead image as the edges appear to have an alternating light and dark pattern. To do this, different galvo scan offset times for different scan speeds will be investigated. Down the road, work can also be done to automate the entire detection system. Using rotation mounts a user could specify the grating angle to image different wavelengths. From there, an additional filter wheel can select the proper filter to further isolate the desired nonlinear signal. There are lots of improvements to be made to the system, but gathering initial images is a helpful starting point.

5. Conclusion

This thesis detailed the design and characterization of a visible, femtosecond pulsed laser source for multiphoton microscopy. The laser emits up to 140mW of light at 520nm with ~100fs pulses, which is more than enough power for multiphoton microscopy. If needed for different applications, further work can be done to improve the efficiency of the 1040nm main amplifier which would increase the power of the frequency doubled beam through the LBO crystal.

The visible MPM was designed with a transmission detection system that uses a diffraction grating to spectrally separate the UV signal from the visible laser source. Further work can be done to improve the detection system, such as selecting mounts and programing them in to LabView to automate the detection based on the desired detection wavelength. Improvements can also be made to improve the efficiency of the detection system and the different wavelengths that may be detected.

Initial images with the system have been captured to prove basic functionality, though the signal is a little bit weak, and the resolution appears low. More work can be done aligning the system and new methods can be made to characterize the resolution. The potential for this instrument is a very high resolution MPM with great application in biological and material sciences.

Works Cited

1. "Laser Scanning Microscopy Tutorial." Accessed March 6, 2020. https://www.thorlabs.com/newgrouppage9.cfm?objectgroup_id=10765.
2. Periasamy, Ammasi, Karsten König, and Peter So. "Special Section Guest Editorial: Thirty Years of Multiphoton Microscopy in the Biomedical Sciences." *Journal of Biomedical Optics* 25, no. 1 (January 2020): 014501. https://doi.org/10.1117/1.JBO.25.1.014501.
3. Göppert-Mayer, Maria. "Über Elementarakte Mit Zwei Quantensprüngen." *Annalen Der Physik* 401, no. 3 (1931): 273–94. https://doi.org/10.1002/andp.19314010303.
4. Kaiser, W., and C. G. B. Garrett. "Two-Photon Excitation in CaF2:Eu2+" *Physical Review Letters* 7, no. 6 (September 15, 1961): 229–31. https://doi.org/10.1103/PhysRevLett.7.229.
5. Denk, Winifried, James H. Strickler, and Watt W. Webb. "Two-Photon Laser Scanning Fluorescence Microscopy." *Science* 248, no. 4951 (April 6, 1990): 73–76. https://doi.org/10.1126/science.2321027.
6. Centonze, Victoria E., and John G. White. "Multiphoton Excitation Provides Optical Sections from Deeper within Scattering Specimens than Confocal Imaging." *Biophysical Journal* 75, no. 4 (October 1, 1998): 2015–24. https://doi.org/10.1016/S0006-3495(98)77643-X.
7. Cromey, Benjamin, R. Dawson Baker, Babak Amirsolaimani, Soroush Mehravar, and Khanh Kieu. "All Reflective Multiphoton Microscope for Use with Compact Multi-Colored Broadband Femtosecond Fiber Lasers." In *Conference on Lasers and Electro-Optics (2017), Paper JTu5A.82*, JTu5A.82. Optica Publishing Group, 2017. https://doi.org/10.1364/CLEO_AT.2017.JTu5A.82.
8. Kieu, K., S. Mehravar, R. Gowda, R. A. Norwood, and N. Peyghambarian. "Label-Free Multi-Photon Imaging Using a Compact Femtosecond Fiber Laser Mode-Locked by Carbon Nanotube Saturable Absorber." *Biomedical Optics Express* 4, no. 10 (October 1, 2013): 2187–95. https://doi.org/10.1364/BOE.4.002187.
9. Kieu, Khanh, and Masud Mansuripur. "Femtosecond Laser Pulse Generation with a Fiber Taper Embedded in Carbon Nanotube/Polymer Composite." *Optics Letters* 32, no. 15 (August 1, 2007): 2242–44. https://doi.org/10.1364/OL.32.002242.
10. Cromey, Benjamin, Ryan J. Knox, and Khanh Kieu. "3D Imaging of Gems and Minerals by Multiphoton Microscopy." *Optical Materials Express* 9, no. 2 (February 1, 2019): 516–25. https://doi.org/10.1364/OME.9.000516.
11. Cromey, Benjamin, Ryan J. Knox, Eric Fritz, and Khanh Kieu. "Exploring Natural Gems and Minerals by Multiphoton Microscopy." In *Light in Nature VII*, 11099:1109902. International Society for Optics and Photonics, 2019. https://doi.org/10.1117/12.2528764.
12. Cromey, Benjamin, Ashley McDaniel, Terry Matsunaga, Josef Vagner, Khanh Quoc Kieu, and Bhaskar Banerjee. "Pancreatic Cancer Cell Detection by Targeted Lipid Microbubbles and Multiphoton Imaging." *Journal of Biomedical Optics* 23, no. 4 (2018): 1–8. https://doi.org/10.1117/1.JBO.23.4.046501.
13. Moulton, P. F. "Spectroscopic and Laser Characteristics of Ti:Al_2O_3." *JOSA B* 3, no. 1 (January 1, 1986): 125–33. https://doi.org/10.1364/JOSAB.3.000125.

14. Zipfel, Warren R., Rebecca M. Williams, and Watt W. Webb. “Nonlinear Magic: Multiphoton Microscopy in the Biosciences.” *Nature Biotechnology* 21, no. 11 (November 2003): 1369–77. https://doi.org/10.1038/nbt899.
15. Seres, Jzsef, Alexander Müller, Enikö Seres, Kevin O’Keeffe, Miklós Lenner, Richard F. Herzog, Daniel Kaplan, Christian Spielmann, and Ferenc Krausz. “Sub-10-Fs, Terawatt-Scale Ti:Sapphire Laser System.” *Optics Letters* 28, no. 19 (October 1, 2003): 1832. https://doi.org/10.1364/OL.28.001832.
16. “Ultrafast Fiber Lasers: An Expanding Versatile Toolbox | Elsevier Enhanced Reader.” Accessed March 21, 2022. https://doi.org/10.1016/j.isci.2020.101101.
17. Qin, Yukun, Orkhongua Batjargal, Benjamin Cromey, and Khanh Kieu. “All-Fiber High-Power 1700 Nm Femtosecond Laser Based on Optical Parametric Chirped-Pulse Amplification.” *Optics Express* 28, no. 2 (January 20, 2020): 2317–25. https://doi.org/10.1364/OE.384185.
18. Nguyen, T. N., K. Kieu, A. V. Maslov, M. Miyawaki, and N. Peyghambarian. “Normal Dispersion Femtosecond Fiber Optical Parametric Oscillator.” *Optics Letters* 38, no. 18 (September 15, 2013): 3616–19. https://doi.org/10.1364/OL.38.003616.
19. “ZEISS Microscopy Online Campus | Microscopy Basics | Numerical Aperture and Resolution.” Accessed March 22, 2022. https://zeiss-campus.magnet.fsu.edu/articles/basics/resolution.html.
20. Ge, Jing, David K. Wood, David M. Weingeist, Somsak Prasongtanakij, Panida Navasumrit, Mathuros Ruchirawat, and Bevin P. Engelward. “Standard Fluorescent Imaging of Live Cells Is Highly Genotoxic.” *Cytometry. Part A : The Journal of the International Society for Analytical Cytology* 83, no. 6 (June 2013): 552–60. https://doi.org/10.1002/cyto.a.22291.
21. Teale, F. W. J., and G. Weber. “Ultraviolet Fluorescence of the Aromatic Amino Acids.” *Biochemical Journal* 65, no. 3 (March 1957): 476–82.
22. Byers, Margaret R. “Dental Sensory Receptors.” In *International Review of Neurobiology*, edited by John R. Smythies and Ronald J. Bradley, 25:39–94. Academic Press, 1984. https://doi.org/10.1016/S0074-7742(08)60677-7.
23. Kollias, Nikiforos, George Zonios, and Georgios N. Stamatas. “Fluorescence Spectroscopy of Skin.” *Vibrational Spectroscopy*, A Collection of Papers Presented at SHEDDING NEW LIGHT ON DISEASE: Optical Diagnostics for the New Millennium, Winnipeg, Canada, June 25-30, 2000, 28, no. 1 (February 28, 2002): 17–23. https://doi.org/10.1016/S0924-2031(01)00142-4.
24. Chappelle, Emmett W., Frank M. Wood, James E. McMurtrey, and W. Wayne Newcomb. “Laser-Induced Fluorescence of Green Plants. 1: A Technique for the Remote Detection of Plant Stress and Species Differentiation.” *Applied Optics* 23, no. 1 (January 1, 1984): 134–38. https://doi.org/10.1364/AO.23.000134.
25. Ehrlich, D. J., P. F. Moulton, and R. M. Osgood. “Ultraviolet Solid-State Ce:YLF Laser at 325 Nm.” *Optics Letters* 4, no. 6 (June 1, 1979): 184–86. https://doi.org/10.1364/OL.4.000184.
26. “Li et al. - UV-FluorescenceSpectroscopy of Coal .Pdf.” Accessed March 22, 2022.

27. “2017 - Fused Silica Transmission Gratings.Pdf.” Accessed March 29, 2022. https://ibsen.com/wp-content/uploads/White-paper-Pulse-stretching-and-compressing-using-grating-pairs_v1.pdf.
28. Ch. Chen, et al., “New Nonlinear Optical Crystal: LiB_3O_5”, J. Opt. Soc. Am. B, Vol. 6, No. 4 (1989)
29. Y. Furukawa, et al., “Investigation of the bulk laser damage of lithium triborate, LiB_3O_5, single crystals”, Appl. Phys. Lett. 65, 1480 (1994)
30. H. Yoshida, et al., “Dependences of Laser-Induced Bulk Damage Threshold and Crack Patterns in Several Nonlinear Crystals on Irradiation Direction” Japanese J. Appl. Phys. Vol. 45, No. 2A, pp. 766–769, (2006)
31. https://www.laser-crylink.com/laser-products/nonlinear-crystal/lbo/
32. https://www.laser-crylink.com/laser-products/nonlinear-crystal/bbo-crystal/
33. Oketani, Ryosuke, Haruka Suda, Kumiko Uegaki, Toshiki Kubo, Tomoki Matsuda, Masahito Yamanaka, Yoshiyuki Arai, Nicholas I. Smith, Takeharu Nagai, and Katsumasa Fujita. “Visible-Wavelength Two-Photon Excitation Microscopy with Multifocus Scanning for Volumetric Live-Cell Imaging.” *Journal of Biomedical Optics* 25, no. 1 (November 2019): 014502. https://doi.org/10.1117/1.JBO.25.1.014502.
34. Kubo, Toshiki, Toshiki Kubo, Kenta Temma, Kenta Temma, Nicholas I. Smith, Kai Lu, Tomoki Matsuda, et al. “Hyperspectral Two-Photon Excitation Microscopy Using Visible Wavelength.” *Optics Letters* 46, no. 1 (January 1, 2021): 37–40. https://doi.org/10.1364/OL.413526.
35. Yamanaka, Masahito, Kenta Saito, Nicholas I. Smith, Yoshiyuki Arai, Kumiko Uegaki, Yasuo Yonemaru, Kentaro Mochizuki, Satoshi Kawata, Takeharu Nagai, and Katsumasa Fujita. “Visible-Wavelength Two-Photon Excitation Microscopy for Fluorescent Protein Imaging.” *Journal of Biomedical Optics* 20, no. 10 (August 2015): 101202. https://doi.org/10.1117/1.JBO.20.10.101202.
36. Ojaghi, Ashkan, Gabriel Carrazana, Christina Caruso, Asad Abbas, David R. Myers, Wilbur A. Lam, and Francisco E. Robles. “Label-Free Hematology Analysis Using Deep-Ultraviolet Microscopy.” *Proceedings of the National Academy of Sciences* 117, no. 26 (June 30, 2020): 14779–89. https://doi.org/10.1073/pnas.2001404117.
37. Kumamoto, Yasuaki, Atsushi Taguchi, and Satoshi Kawata. “Deep-Ultraviolet Biomolecular Imaging and Analysis.” *Advanced Optical Materials* 7, no. 5 (2019): 1801099. https://doi.org/10.1002/adom.201801099.
38. Maity, Barun Kumar, and Sudipta Maiti. “Label-Free Imaging of Neurotransmitters in Live Brain Tissue by Multi-Photon Ultraviolet Microscopy.” *Neuronal Signaling* 2, no. 4 (December 3, 2018): NS20180132. https://doi.org/10.1042/NS20180132.
39. Balaji, J., Chandra S. Reddy, S. K. Kaushalya, and Sudipta Maiti. “Microfluorometric Detection of Catecholamines with Multiphoton-Excited Fluorescence.” *Applied Optics* 43, no. 12 (April 20, 2004): 2412–17. https://doi.org/10.1364/AO.43.002412.
40. Sarkar, Bidyut, Arkarup Banerjee, Anand Kant Das, Suman Nag, Sanjeev Kumar Kaushalya, Umakanta Tripathy, Mohammad Shameem, Shubha Shukla, and Sudipta Maiti. “Label-Free Dopamine Imaging in Live Rat Brain Slices.” *ACS Chemical Neuroscience* 5, no. 5 (May 21, 2014): 329–34. https://doi.org/10.1021/cn5000138.